

**THE (n,2p) REACTION AS A
PROBE FOR A NUCLEAR Δ^{++}
COMPONENT**

By

Rachel J. De Young

A thesis submitted in partial fulfillment of the
requirements for the degree of

Bachelor of Science

Houghton College

May 2003

Signature of Author.....

Department of Physics
May 19, 2003

.....

Dr. Mark Yuly
Associate Professor of Physics
Research Supervisor

.....

Dr. Ronald Rohe
Associate Professor of Physics

**THE (n,2p) REACTION AS A
PROBE FOR A NUCLEAR Δ^{++}
COMPONENT**

By

Rachel J. De Young

Submitted to the Department of Physics
on May 19, 2003 in partial fulfillment of the
requirement for the degree of
Bachelor of Science

Abstract

An experiment to measure the ${}^3\text{He}(n,2p)2n$ and ${}^4\text{He}(n,2p)3n$ cross-sections was conducted at the Los Alamos Neutron Science Center (LANSCE) as a means to explore the Δ^{++} contribution to the nuclear wave function. Neutrons incident on gaseous ${}^3\text{He}$ and ${}^4\text{He}$ targets produced outgoing protons which traveled through two magnetic spectrometer arms, each consisting of a thin ΔE plastic scintillator, a permanent bending dipole magnet, two sets of x-y drift chambers, and a final calorimeter of three stacked plastic scintillators. Computer codes are being developed to analyze the delay line readouts from the drift chambers in order to determine particle trajectories through the magnetic field and trace back to the target. This information will be used to identify the outgoing particles and calculate their momenta. Once cross-sections have been determined, comparisons may be made to theoretical predictions that include a Δ component to the nuclear wave function.

Thesis Supervisor: Dr. Mark Yuly
Title: Associate Professor of Physics

TABLE OF CONTENTS

Chapter 1 Introduction.....	6
1.1 Description of the Δ Particle	6
1.2 History and Motivation.....	6
1.3 Previous Experiments.....	9
1.3.1 Pion Double Charge Exchange.....	9
1.3.2 Previous (n,2p) Experiment.....	9
1.3.3 Electromagnetic Investigations	11
1.4 The (n,2p) Experiment	12
Chapter 2 Experiment.....	13
2.1 Overview	13
2.2 Proton Beam.....	13
2.2.1 Cockroft-Walton Ion Injectors	13
2.2.2 Drift Tube LINAC	14
2.2.3 Side-Coupled-Cavity LINAC.....	15
2.2.4 Time Structure of Proton Beam.....	16
2.3 Neutron Beam.....	16
2.4 The (n,2p) Experiment	17
2.4.1 Fission Chamber	17
2.4.2 Gaseous ^3He and ^4He Targets	19
2.4.3 ΔE Detectors	19
2.4.4 Drift chambers	21
2.4.5 Permanent Magnets	23
2.4.6 Scintillating Calorimeters	23
2.5 Electronics.....	24
Chapter 3 Analysis.....	26
3.1 Drift Chamber Analysis	26
3.2 Charged Particle Position in Drift Chamber	26
3.2.1 Anode Wire Position.....	26
3.2.2 Electron Drift Distance	30
3.2.3 Cathode Pulses	32
3.3 Position with Respect to the Beam Line.....	34

Chapter 4 Conclusions	38
Appendix A Scale Drawing of Apparatus.....	39
Appendix B Complete Electronics Diagrams	50
Appendix C Description of Computer Codes	60
C.1 Overview	60
C.2 Conversion from XSYS to ROOT.....	60
C.3 Determining Event Position Within Drift Chamber	60
C.3.1 Cuts Applied During Analysis	61
C.3.2 Drift Chamber Coefficients	61
C.3.3 Determine Drift Distance	61
C.3.4 Resolution of Left-Right Ambiguity.....	62
C.4 Location of Events with Respect to Beam Line	62
Appendix D Cuts Applied to Data	63

TABLE OF FIGURES

Figure 1. Schematic diagram of the two step (n,2p) reaction.....	7
Figure 2. Schematic diagram of the one step (n,2p) reaction.....	8
Figure 3. Monte Carlo simulation of the missing energy spectrum.....	10
Figure 4. Measured missing energy spectrum.....	11
Figure 5. An aerial view of LANSCE.....	14
Figure 6. Schematic diagram of a typical Cockroft-Walton generator.....	15
Figure 7. Schematic diagram of a typical drift tube LINAC.....	16
Figure 8. An artist's representation of the WNR facility.....	17
Figure 9. Schematic diagram of the (n,2p) experiment.....	18
Figure 10. Photograph of the experimental area.....	19
Figure 11. Schematic diagram of a photomultiplier tube.....	20
Figure 12. Schematic diagram of a drift chamber.....	22
Figure 13. Electronics diagram showing the trigger.....	24
Figure 14. Schematic diagram showing a charged particle passing through a drift chamber plane.....	27
Figure 15. Schematic diagram illustrating the difference in signal path length.....	27
Figure 16. Typical histogram of wire position.....	29
Figure 17. Plot of integrated counts per time.....	31
Figure 18. Histogram of the output from the ADC.....	32
Figure 19. Schematic diagram of a charged particle passing through a drift chamber plane.....	33
Figure 20. The four possible configurations for adding or subtracting drift distances.....	34
Figure 21. Schematic of the placement of the lead bricks in front of the drift chambers.....	35
Figure 22. Plot of plane x versus plane y for the first drift chambers.....	36
Figure 23. Plot of plane x versus plane y for the rearmost drift chambers.....	37
Figure 24. Determining the location of the lead brick	63

Chapter 1

INTRODUCTION

1.1 Description of the Δ Particle

The purpose of this experiment is to explore the possible contribution of a Δ^{++} component to the nuclear wave functions for ${}^3\text{He}$ and ${}^4\text{He}$. Before beginning a discussion of this experiment, a brief description of the characteristics of the Δ will be given.

Δ particles are nucleon resonance structures. The Δ particles under consideration in this experiment are the lowest energy resonance structures possible with a mass of approximately $1232 \text{ MeV}/c^2$ and spin and isospin of $3/2$ [1]. There are four different charge configurations for the Δ , as shown in Table 1.

Table 1. Properties of Δ particles [1].

	Rest Mass (MeV/c^2)	Quark Content	Spin	Isospin
Δ^{++}	1230.5-1231.1	uuu	3/2	3/2
Δ^+	1231.2-1234.9	uud	3/2	3/2
Δ^0	1233.1-1233.8	udd	3/2	3/2
Δ^-	1232 ¹	ddd	3/2	3/2

¹The mass for Δ^- has not yet been determined experimentally [1].

1.2 History and Motivation

Traditional models of the nucleus that treat it as a non-relativistic system of nucleons do not completely explain the binding energies and the electromagnetic properties of nuclei [2]. In the 1960s, theorists suggested the presence of virtual pre-existing Δ (1232 MeV) particles in ground-state nuclear wave functions and that this Δ resonance might be important in explaining nuclear structure [3].

It has proven difficult to observe the signature of a Δ component to the nuclear wave function because most previous experimental work has probed for a Δ component by knocking Δ particles out of the nucleus. In these reactions it is difficult to distinguish the preexisting Δ particles from those created in the reaction [4]. In order to measure the contribution to the cross section due to Δ particles in the nucleus, reactions that are otherwise highly suppressed are being studied. This thesis describes measurements of the Δ^{++} contribution to the cross section for two such reactions, ${}^3\text{He}(n,2p)2n$ and ${}^4\text{He}(n,2p)3n$.

In the ${}^3\text{He}(n,2p)2n$ reaction a neutron (n) was incident on a ${}^3\text{He}$ nucleus. The outgoing particles from the event were two protons (p), which were detected, and two neutrons.

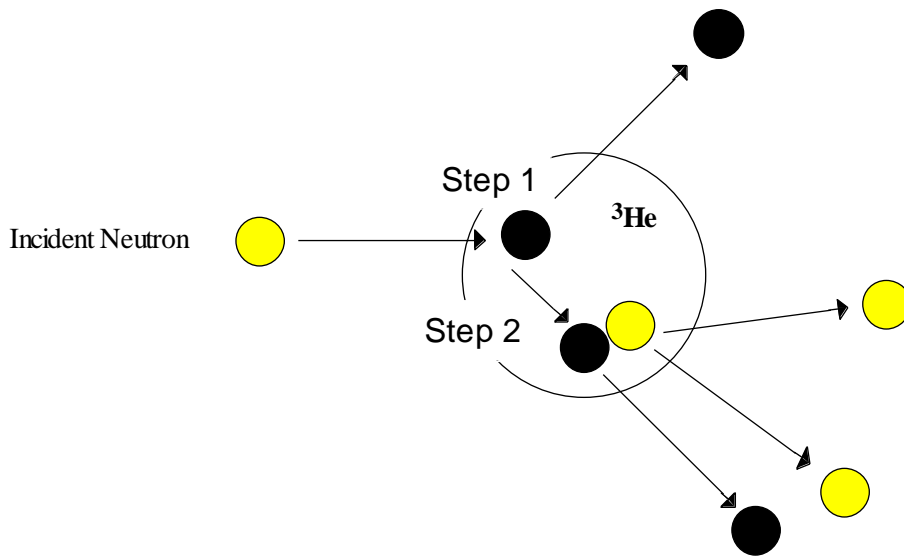


Figure 1. Schematic diagram of the two step $(n,2p)$ reaction. In a ${}^3\text{He}$ nucleus with two protons (black) and a neutron (gray), the $(n,2p)$ reaction may occur in two steps with the incident neutron interacting with each proton separately.

In the ${}^4\text{He}(n,2p)3n$ reaction two outgoing protons were still detected, but there were three outgoing neutrons. These $(n,2p)$ reactions may proceed in two steps if the nucleus contains only two protons. The incident neutron may interact with each proton in turn, as shown in Figure 1. However, if the

incident neutron interacts with a nuclear Δ^{++} , the reaction may proceed in one step. The neutron may interact with the Δ^{++} , which will then decay into two protons as shown in Figure 2.

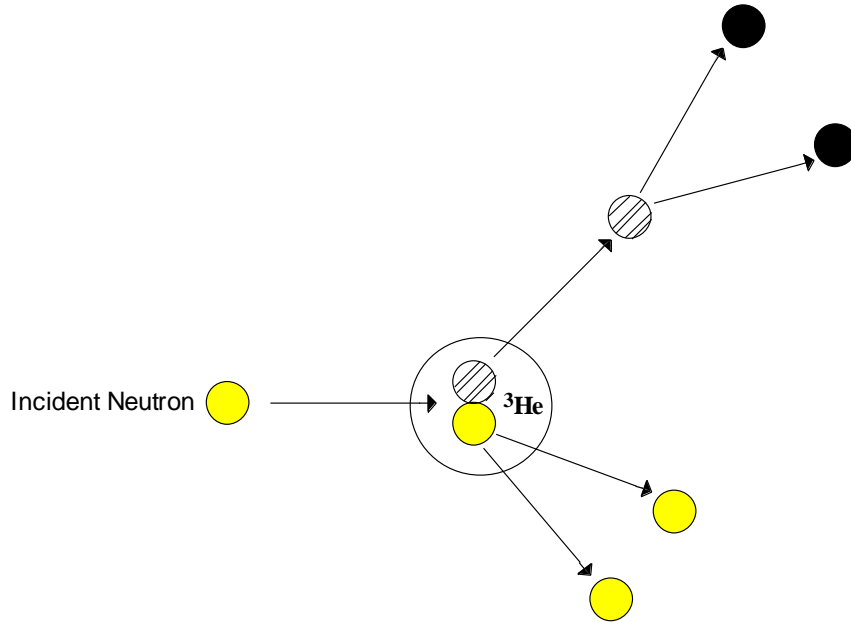


Figure 2. Schematic diagram of the one step (n,2p) reaction. In a ³He nucleus containing a Δ^{++} particle (striped), the incident neutron (gray) scatters quasi-elastically from the Δ^{++} which then decays into two protons (black).

In each of these cases the kinematical angles and energies of the outgoing particles are different. The difference between the incident neutron energy and the energies of the two protons plus the energy of the reaction, called the missing energy, may be found for the interactions. The missing energy is defined as $T_{\text{miss}} = T_n - Q - T_{2p}$ where T_{miss} is the missing energy, T_n is the energy of the incident neutron and T_{2p} is the energy of the two protons. A missing energy spectrum for the reaction is expected to have a peak due to the quasi-free scattering of two particles interacting elastically as if there were no forces binding them to nuclei. The width and shape of the quasifree peak is a result of interactions with spectator and already scattered nucleons. In this experiment, a quasi-free two body scattering peak may indicate a possible Δ component to the nuclear wave function.

1.3 Previous Experiments

Past experiments examining the contribution of Δ particles to the nuclear wave function have looked at various reactions that are highly suppressed in nuclei not containing a Δ component. These have included pion double charge exchange experiments, previous work with the $(n,2p)$ reaction, and pion photo- and electro- production. Each of these will be examined in more detail.

1.3.1 Pion Double Charge Exchange

Morris *et. al.* [5] studied the Δ^- component in ^3He , ^4He , ^6Li , ^7Li , ^{12}C , ^{13}C , ^{90}Zr , and ^{208}Pb nuclei using the $(\pi^+, \pi^- p)$ double charge exchange reaction in which an incident π^+ interacts with a nucleus and an outgoing π^- and proton are detected in coincidence. Like the $(n,2p)$ reaction, the $(\pi^+, \pi^- p)$ reaction will generally proceed in two steps in nuclei consisting of only nucleons. The incident π^+ exchanges one unit of charge with a neutron in the nucleus, leaving a π^0 and a proton. The π^0 then exchanges charge with another neutron and the resulting π^- and proton leave the nucleus. With a Δ^- component, the reaction may proceed in one step. In the one step reaction, the incident π^+ exchanges two units of charge with the Δ^- , producing a π^- and a Δ^+ . The Δ^+ then decays into a proton and a neutron and the outgoing π^- and proton are detected in coincidence. As with the $(n,2p)$ reaction, when the reaction takes place in one step, two-body quasi-free scattering should dominate and its characteristic peak should be observable in the missing energy spectrum [5]. The recoiling particle from the reaction should be emitted close to the angle expected for free-body scattering with some spread due to differences in the initial momentum of the Δ^- particle [5].

These measurements [5] of the pre-existing nuclear Δ^- component seem to indicate a 1-3% Δ^- component to the nuclear wave function. This is consistent with theoretical predictions by Green [6].

1.3.2 Previous $(n,2p)$ Experiment

In 1996 and 1997, the $^3\text{He}(n,2p)2n$ and $^4\text{He}(n,2p)3n$ reactions were studied at the Weapons Nuclear Research facility (WNR) of the Los Alamos Neutron Science Center (LANSCE) by a collaboration

from Massachusetts Institute of Technology (MIT), Thomas Jefferson National Accelerator Facility (TJNAF), and Los Alamos National Laboratory (LANL). In this experiment, incident neutrons from the neutron beam provided by LANSCE passed through a fission chamber that monitored neutron flux, then interacted with gaseous ^3He and ^4He targets that were contained in aluminum gas cylinders. Outgoing particles were detected in two ΔE - E scintillator telescopes that were placed on opposite sides of the beam line at angles of 40° and 50° [7]. Insufficient events were detected to determine a statistically meaningful cross section for the Δ^{++} component to the nuclear wave function, but the results do seem to suggest a possible nuclear Δ^{++} component [7].

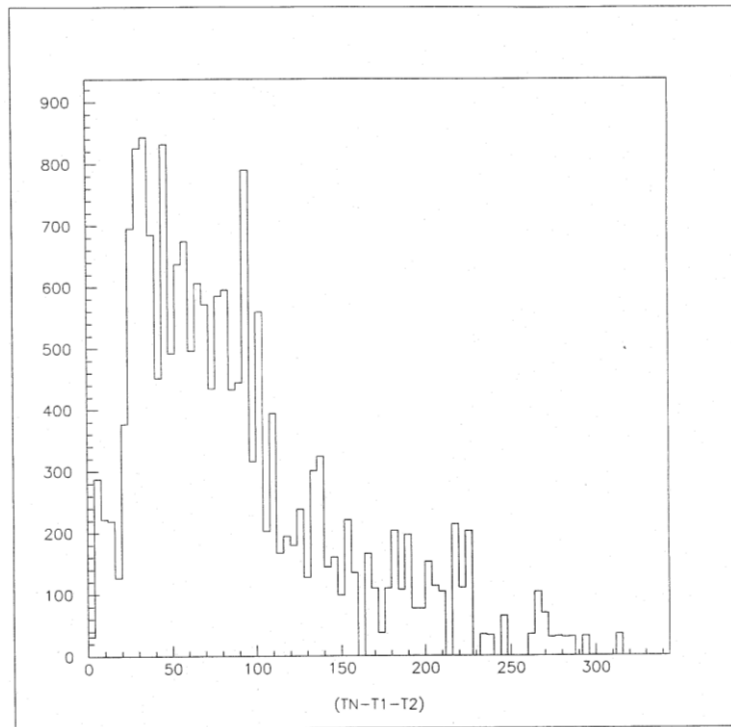


Figure 3. Monte Carlo simulation of the missing energy spectrum for accidental two proton coincidences. Notice the broad peak around 50 MeV.

In Monte Carlo simulations of the missing energy spectrum for accidental two proton coincidences, there is a broad peak about 50 MeV, as may be seen in Figure 3 [4]. The measured missing energy

spectrum has a sharp peak around 50 MeV, as in Figure 4 [4]. This seems to indicate that the sharp peak around 50 MeV in the measured missing energy spectrum may correspond to a two-body quasi-free reaction as would be expected for the one-step interaction between an incident neutron and a Δ^{++} particle.

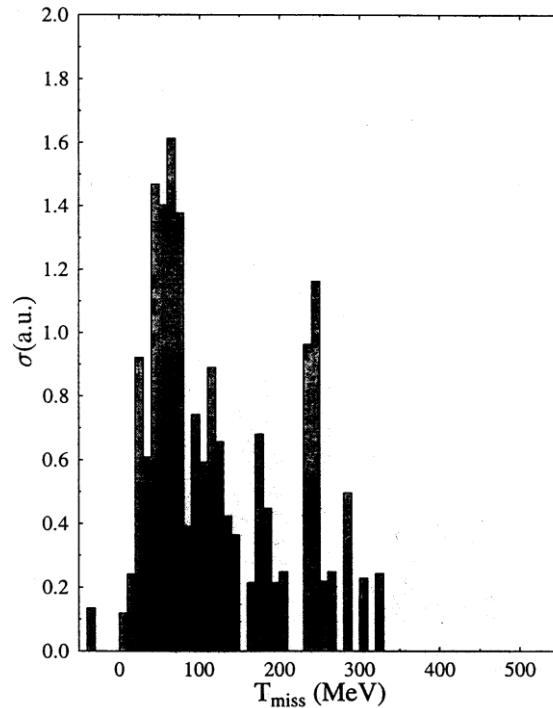


Figure 4. Measured missing energy spectrum showing a sharp peak around 50 MeV. There is an unidentified sharp peak around 260 MeV.

1.3.3 Electromagnetic Investigations

Two previous experiments probed the nuclear Δ component by looking at pion photo- and electro-production. Emura *et. al.* [8] used the ${}^3\text{He}(\gamma, p\pi^\pm)$ reaction to investigate the Δ^{++} and Δ^0 component to the nuclear wave function for ${}^3\text{He}$. Analysis indicated a Δ contribution to the nuclear wave function of less than a 2% [8]. Based on theoretical predictions by Lipkin and Lee [9], Milner and Donnelly [10] suggested using the polarized ${}^3\text{He}(e, e'\pi^\pm)$ reaction to search for a Δ component to the nuclear wave

function. These investigations would use the asymmetry in spin-dependent scattering, which leads to an enhancement of the longitudinal electroproduction cross section [10]. A measurement of the asymmetries $A(\pi^\pm)$ on the ${}^3\text{He}(e,e'\pi^\pm)$ processes is currently underway at the Bates Large Acceptance Spectrometer Toroid (BLAST) facility at MIT.

Taken together, the (π^+, π^-p) , $(n, 2p)$, and electromagnetic interactions seem to support the idea of a pre-existing Δ component to the nuclear wave function.

1.4 The $(n, 2p)$ Experiment

Following the suggestive results obtained in 1996 and 1997, the $(n, 2p)$ experiment was redesigned in 1998 to increase the detector solid angle and enhance the energy resolution. In this way, it was hoped that measurements could be made for a wider range of incident neutron energies [7]. To accomplish this, the ΔE - E scintillators were replaced by magnetic spectrometers 45° to the left and right of the beam line. By improving the detector solid angle and enhancing the energy resolution, the magnetic spectrometers were expected to produce a more defined quasi-free peak in the missing energy spectrum [7]. The redesigned experiment was carried out in 1999 and 2000 and data analysis is currently underway.

Chapter 2

EXPERIMENT

2.1 Overview

To probe the Δ^{++} component of the ${}^3\text{He}$ and ${}^4\text{He}$ nuclear wave functions, an experiment was performed at the Weapons Nuclear Research (WNR) facility of the Los Alamos Neutron Science Center (LANSCE) in Los Alamos, New Mexico. The LANSCE facility uses the remnants of the Los Alamos Meson Physics Facility (LAMPF) which was used to produce pion beams. At LANSCE, the Clinton B. Anderson linear accelerator (LINAC) provides a 1-milliampere, 800 MeV proton beam for use in nuclear physics research. The WNR facility was built adjacent to the LINAC, as may be seen in the aerial photograph of Figure 5, to house experiments requiring intense neutron beams for nuclear weapon design research as well as non-defense related nuclear physics experiments such as the (n,2p) experiment.

The ordering of the subsequent discussion of the experimental apparatus for the (n,2p) experiment will follow the beam as it traveled down the LINAC and through the experimental area.

2.2 Proton Beam

The Clinton B. Anderson LINAC produced the proton beam, which in turn produced the neutron beam. The LINAC consists of three stages: the ion injectors, the drift-tube LINAC, and the side-coupled cavity LINAC.

2.2.1 *Cockcroft-Walton Ion Injectors*

The first stage of the LINAC is two 750 keV Cockcroft-Walton generators with ion sources located inside their high voltage terminals.



Figure 5. An aerial view of LANSCE. The linear accelerator is in the background and the WNR facility is in the foreground.

One ion source strips hydrogen atoms of their electrons to form H^+ and one adds electrons to hydrogen atoms to form H^- [11]. The generators themselves consist of rectifiers which charge capacitors in parallel and discharge them in series [12], as may be seen in Figure 6. These five capacitors charge during a half cycle and transfer the charge during the next half cycle, resulting in a steady potential of 750 kV at the terminals [12].

2.2.2 *Drift Tube LINAC*

The potential difference between the generators and the drift tube LINAC, which is the second stage, accelerates the ions to 750 keV. The H^+ and H^- ions are injected in alternating bunches into the 201.25 MHz drift tube LINAC where they are accelerated to 100 MeV. As can be seen in Figure 7, when the charged particles pass through the drift tube LINAC, the alternating polarities on the drift tubes oscillate at 201.25 MHz, causing them to accelerate.

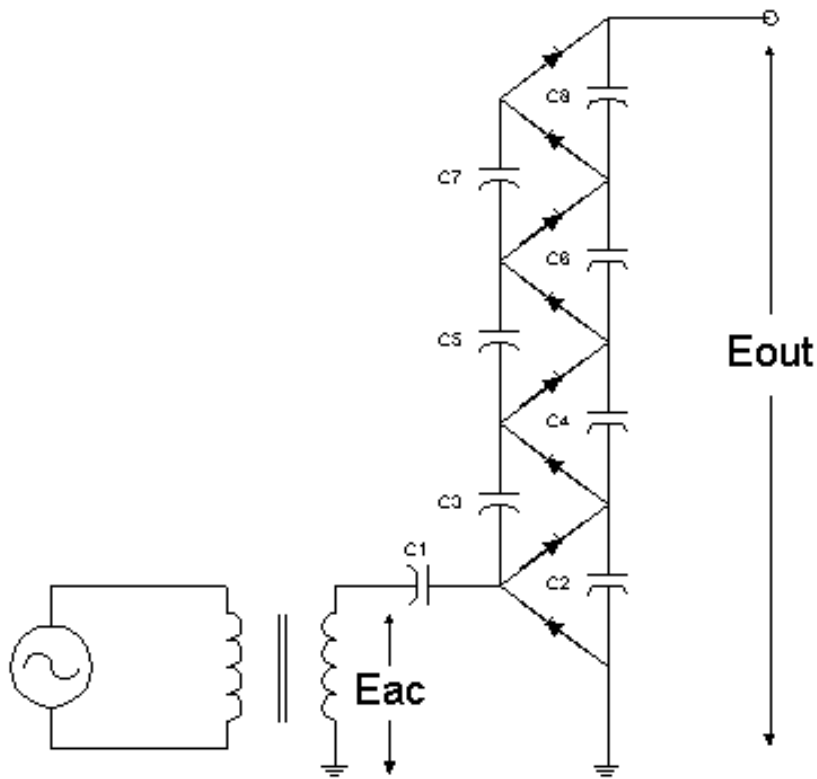


Figure 6. Schematic diagram of a typical Cockcroft-Walton generator showing the capacitors that charge in parallel and discharge in series. The generators for the Clinton B. Anderson LINAC consist of 5 capacitors and reach 750 kV at the terminals [12].

As the particles gain energy, the drift tubes become longer so that the particles spend the same amount of time in each tube. This lengthening of the drift tubes decreases as the effects of relativity becomes more noticeable because at higher energies the increase in mass of the particle is more significant than the increase in velocity.

2.2.3 Side-Coupled-Cavity LINAC

From the drift tube LINAC, the beam passes into the third stage, the 800-meter side-coupled-cavity LINAC. Here the particles accelerate to their final energies of 800 MeV. The side-coupled-cavity LINAC operates in much the same way as the drift tube LINAC.

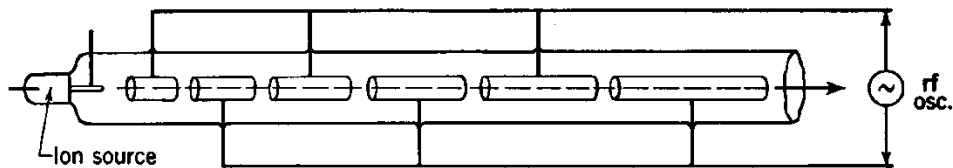


Figure 7. Schematic diagram of a typical drift tube LINAC. Ions from the ion source are accelerated through the increasingly long tubes by alternating potentials on the tubes. This figure was taken from Ref. [12].

2.2.4 Time Structure of Proton Beam

The maximum average current for the proton beam is 0.8 mA. The proton beam is pulsed and each of these macropulses lasts 900 μ s. The macropulses have micropulses of 0.25 ns bursts of protons separated by 5 ns [13].

2.3 Neutron Beam

The neutron beam is produced when the proton beam from the LINAC is accelerated into a spallation target. As shown in Figure 8, the proton beam is diverted slightly into the Target 4 area where it interacts with an 3 cm x 7.5 cm unmoderated tungsten spallation source [14]. Neutrons and protons scatter in every direction with energies ranging from 0 to 750 MeV. Some of the neutrons and protons enter the seven collimated beam lines leading to different experimental areas. Magnetic fields bend the paths of protons into the collimators, but because neutrons have no charge, they pass through the collimators unaffected.

The (n,2p) experiment was located 90 meters from the spallation source, at the end of the flight path 15° to the left of the beam line (FP15L), as shown in Figure 8. The time for neutrons to travel the known distance from the spallation source to the target (91.2 m) is called the neutron time of flight (NTOF). Since the proton beam is evenly pulsed, the start time is known, while the arrival time is

determined by a coincidence of signals in one of the ΔE detectors and both of the calorimeters (see Section 2.5). Once the NTOF is known, the energies of the incident neutrons may be determined.

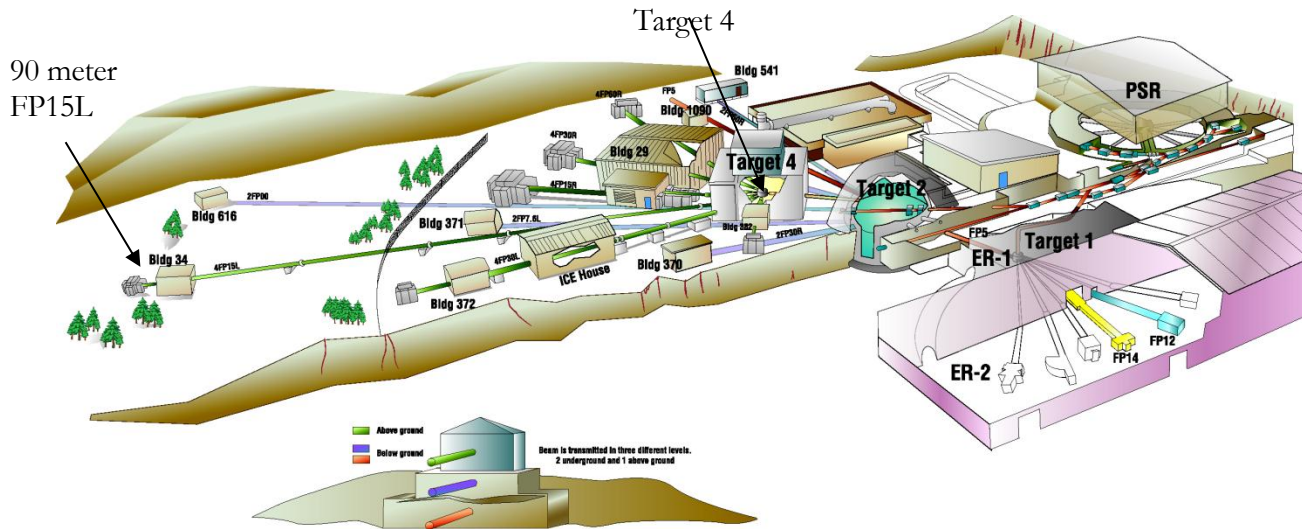


Figure 8. An artist's representation of the WNR facility. The proton beam enters the Target 4 area and interacts with an unmoderated tungsten spallation source. Outgoing neutrons travel down different flight paths. The $(n,2p)$ experiment was located on the 90-meter flight path 15L as shown (figure from Ref. [14]).

2.4 The $(n,2p)$ Experiment

The experimental apparatus was designed to detect in coincidence two outgoing protons from a ^3He or ^4He target. It consisted of a ^3He or ^4He gaseous target and two magnetic spectrometers: one 45° to the left and one 45° to the right of the beam line. As may be seen in Figure 9 and Figure 10, each magnetic spectrometer consisted of a thin ΔE plastic scintillator, a set of drift chambers, a permanent bending magnet, another set of drift chambers, and a final calorimeter of three stacked plastic scintillators.

2.4.1 Fission Chamber

Neutrons entering the experimental area first passed through the fission chamber. The fission chamber

was lined with the fissile isotope ^{238}U and filled with a gas mixture including argon and isobutane [15]. A potential difference of 290 V existed between the two end plates of the chamber. When neutrons entered, a small fraction interacted with the lining and fission occurred. The fission fragments ionized the gas as they passed through the chamber. The electrons released during ionization were attracted to the positive plate and created a current which varied with the number of incident neutrons. Since the current was proportional to the number of neutrons entering the experimental area, the fission chamber allowed the neutron flux to be monitored.

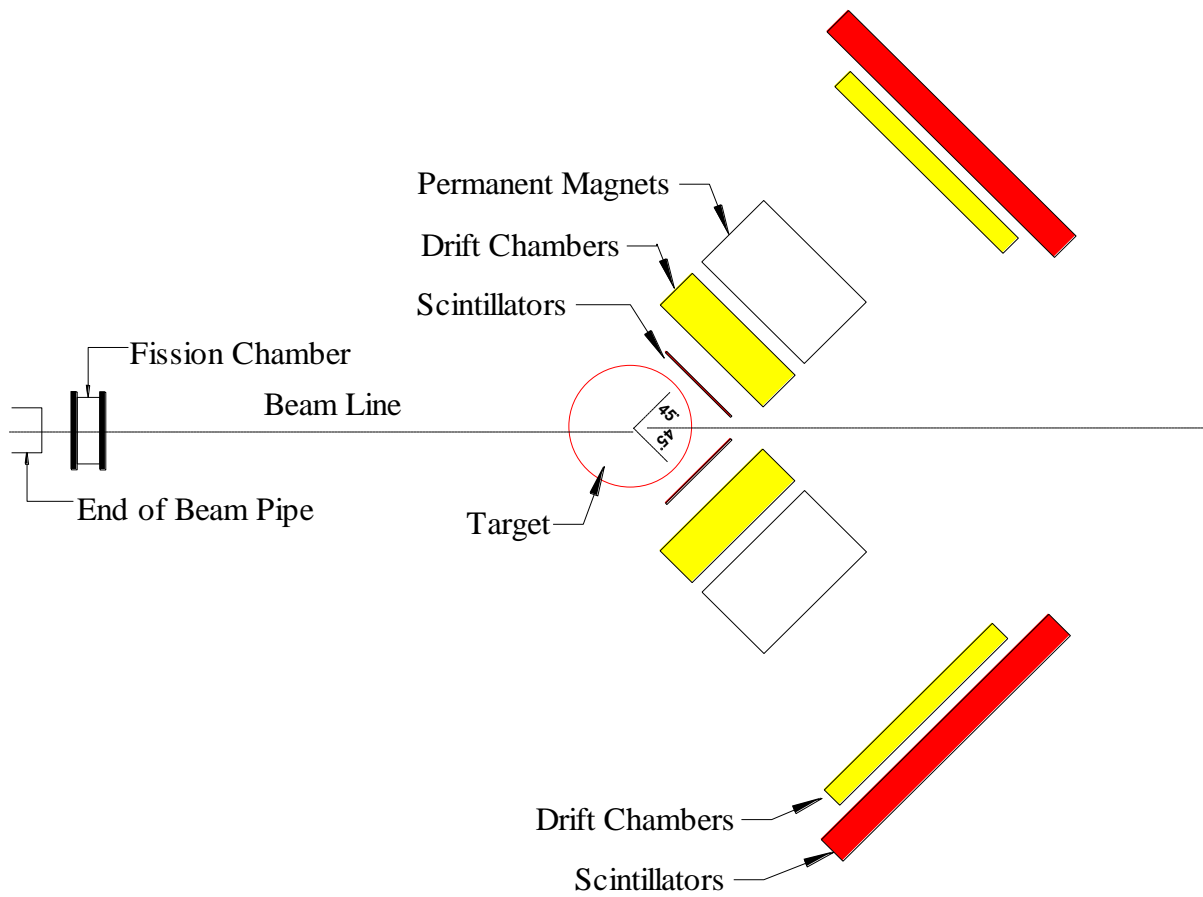


Figure 9. Schematic diagram of the (n,2p) experiment. Outgoing protons from the target were detected in the magnetic spectrometers to the left and right of the beam line. For a scale drawing, see Appendix A.

Neutrons that passed through the fission chamber continued along the beam line toward the target, as shown in Figure 9.

2.4.2 Gaseous ^3He and ^4He Targets

The gaseous ^3He and ^4He targets were contained in aluminum gas cylinders kept at 10.27 and 13.46 MPa respectively. Each aluminum cylinder had a diameter of 0.206 meters.

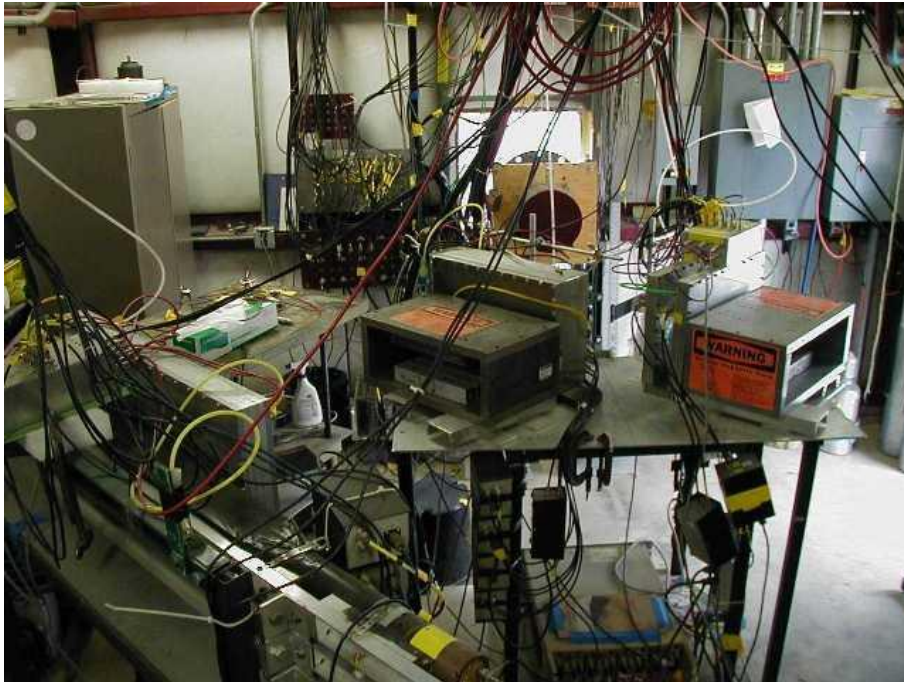


Figure 10. Photograph of the experimental area. The neutron beam entered through the beam pipe in the back and passed through the target, which was removed at the time of the photograph. Outgoing particles were detected in the magnetic spectrometers to the left and right of the beam line.

2.4.3 ΔE Detectors

Outgoing protons from the interactions of incident neutrons with ^3He or ^4He nuclei first passed through ΔE scintillators, which were used to reduce background events. Each consisted of a plastic scintillator 33 cm (left of beam line) or 30.5 cm (right of beam line) long and 4.9 cm high attached via a

light guide to a photomultiplier tube (PMT). Charged particles passing through the scintillator excited molecules to a higher energy state. The molecules released some of this energy through lattice vibrations, and may have then transition to a minimum energy state by emitting photons.

The PMT converted these light pulses into electrical signals. The operation of the PMT is illustrated in Figure 11. The tube absorbed the light from the scintillator at the photocathode, which was kept at a high voltage. The energy from this light pulse ejected electrons from the photocathode via the photoelectric effect. The electrons were attracted to dynodes, which were kept at successively lower potentials, so that the electrons were accelerated across potential differences.

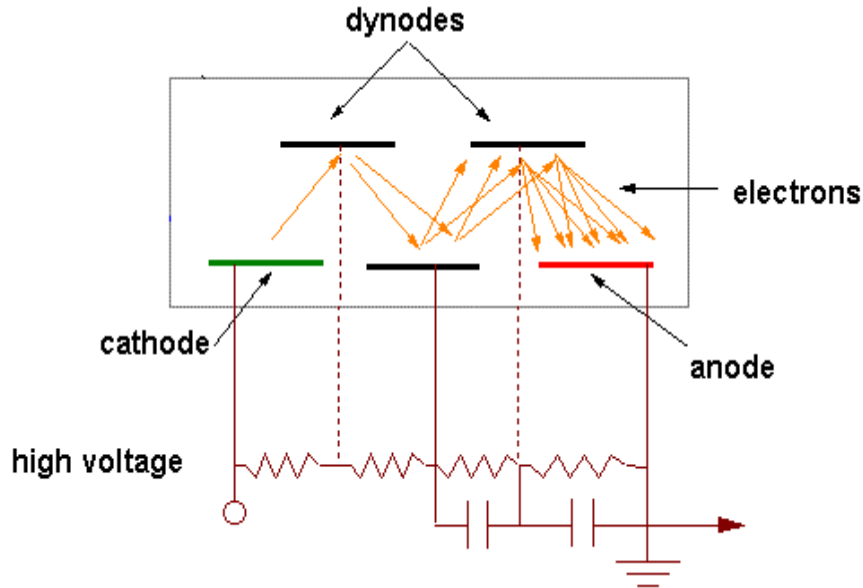


Figure 11. Schematic diagram of a photomultiplier tube. Photons from the plastic scintillator were converted to an electrical signal when the photons ejected electrons from the photocathode and these electrons ejected more electrons from each successive dynode.

As electrons struck the successive dynodes, more and more electrons were released and accelerated through a potential difference toward the next dynode. This cascade continued through all the

dynodes until the electrons reached the anode where the amplified pulse of current exited the photomultiplier tube to be recorded.

Since the ΔE detectors were so thin, charged particles that interacted in the plastic scintillator lost very little energy. Uncharged particles such as neutrons that might have passed through the ΔE detectors were very unlikely to interact, and therefore a coincidence signal in the ΔE and in the calorimeter in the back of the experiment indicated an event most likely due to a charged particle.

2.4.4 *Drift chambers*

After passing through the ΔE detectors, outgoing particles from the target entered the first set of drift chambers. There were two sets of drift chambers in each magnetic spectrometer, one before the permanent bending magnet and one after. The drift chambers before and after each permanent magnet provided the two points necessary to find the trajectories of the charged particles before and after they passed through the magnetic fields of the permanent magnets.

The sets of drift chambers consisted of two drift chambers separated by approximately 7 cm. Each drift chamber consisted of an x plane formed by vertical anode wires and a y plane formed by horizontal anode wires. The anode wires formed a grid so that the location of the passage of a charged particle through the chamber could be determined. The anode wires were spaced every 8 mm. Centered between anode wires were cathode wires, as shown in Figure 12. The chambers were sealed on the sides by a 6.3 μm mylar foil that was aluminized on both sides and epoxied to the cathode plane frames. The cathode frames were also held at ground [16]. The chambers were filled with gaseous mixture predominately of argon and isobutane. As charged particles passed through the chambers, they ionized the gas along their paths. Freed electrons drifted to the nearest anode wire, which was held at a positive high voltage between 2070 V and 2160 V depending on the plane, and induced a pulse. The pulse passed down the anode wire to a delay line, as can be seen in Figure 12, and then traveled along the delay line in each direction to the time to FERA converters (TFCs) at the ends of the wires. The time difference between the start of the micropulse from the proton beam and the arrival of a signal pulse in a TFC was recorded if there was a coincidence signal in one ΔE detector

and both scintillating calorimeters, described in Section 2.5. There was typically a difference in times between the arrival of signals in the left and in the right TFCs since it took varying amounts of time for the signals to travel the different lengths of delay line to each TFC. This time difference was used to determine which anode wire the charged particle was nearest.

There were also pulses in the cathode wires on either side of the anode wire nearest to the event. The cathode wire on one side of an anode wire, called the “odd” cathode wire, was bussed together with all the “odd” cathode wires and the cathode wire on the other side of the anode wire (“even” cathode wire) was bussed with the “even” cathode wires, as seen in Figure 12. The pulse was larger in the cathode wire nearest to where the particle passed through the chamber. Signals from the odd and even cathode wires passed into a differential amplifier which produced a pulse proportional to the difference between the two input signals. Depending on the size of the pulses, the differential amplifier output was positive or negative, indicating on which side of the anode wire an event occurred.

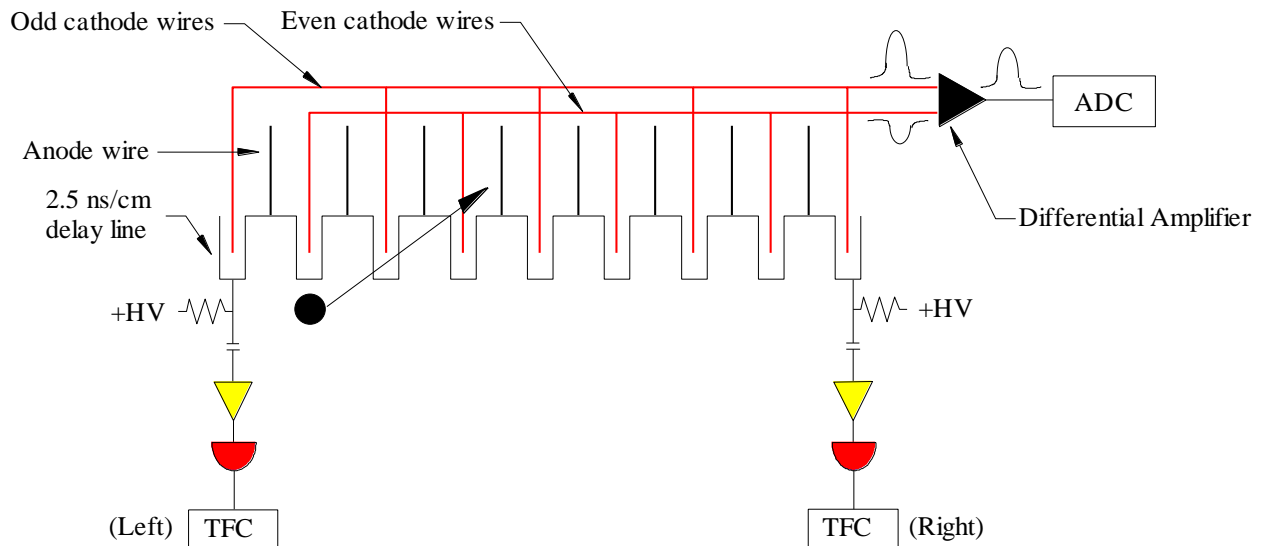


Figure 12. Schematic diagram of a drift chamber. As a charged particle (shown in black) passed through the drift chamber, it ionized the gas and induced pulses in the anode and cathode wires.

The outputs from the drift chambers were then used to determine the locations of the charged particles as they passed through the chamber, as will be discussed in Chapter 3.

2.4.5 *Permanent Magnets*

From the first set of drift chambers, the charged particles passed between the poles of the 30 cm x 48 cm samarium-cobalt permanent magnets. Particles with charge q in a magnetic field \vec{B} experience a force

$$\vec{F} = q\vec{v} \times \vec{B} \quad (2.1)$$

and travel in a helical pattern. The component of the force parallel to the velocity keeps the charged particles circling. Since the force required to keep objects moving in a circle is

$$F = mv^2/r \quad (2.2)$$

where r is the radius, the relationship between the velocity and the radius for a charged particle in a magnetic field may be found by setting Eq. 2.2 equal to the component of Eq. 2.1 that is parallel to the velocity,

$$mv = qBr. \quad (2.3)$$

The momentum is mv , so Eq. 2.3 may be rewritten as

$$p = qBr. \quad (2.4)$$

Thus the momenta of the charged particles may be found by using the drift chambers before and after the permanent magnets to determine the radius of the arc as the charged particles pass through the magnetic field.

2.4.6 *Scintillating Calorimeters*

The charged particles deposited their remaining energy in the calorimeters, located in the foreground

of Figure 10. Each calorimeter consisted of a stack of three 10.1 cm x 10.1 cm x 106.5 cm plastic scintillators with photomultiplier tubes on each end. The size of the pulse from each PMT was proportional to the energy deposited in the scintillator, so it acted as a check for the energy determination using the drift chambers. Also, the computer was triggered to record data whenever an event was detected in one of the ΔE scintillators and both of the calorimeters.

2.5 Electronics

The electronics processed signals from the detectors and drift chambers before passing them to the computer for storage. Triggering the electronics required detection of a proton in one arm and a neutron in the other, or of a proton in each arm. A proton passing through a magnetic spectrometer would typically induce signals in the ΔE detector and in the calorimeter whereas a neutron would typically only induce a signal in the calorimeter (see 2.4.3).

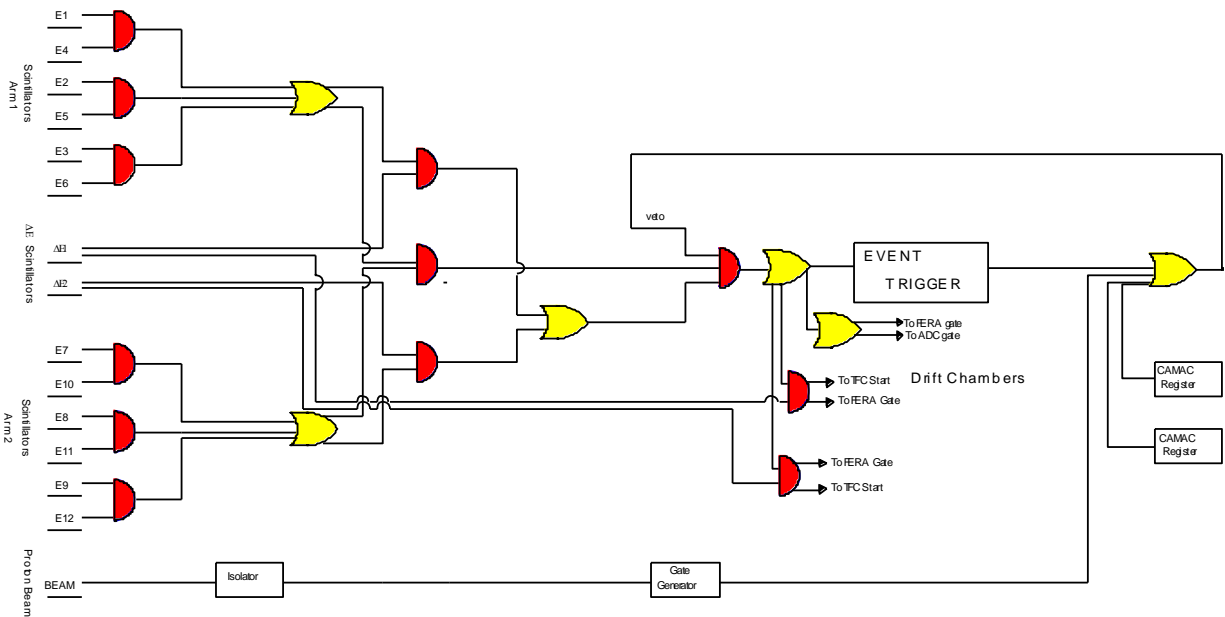


Figure 13. Electronics diagram showing the trigger. If the beam or the CAMAC registers were turned off or if the computer was busy, the trigger was vetoed. For more complete electronics diagrams, see Appendix B.

Thus, triggering the electronics required detection of a charged particle passing through one of the ΔE detectors and a coincidence of signals from the calorimeters in each arm. Since an event was required in each calorimeter, the trigger further ensured that two charged particles had passed through the spectrometers at approximately the same time, which increased the probability that the events were from outgoing particles from the target. As can be seen in the electronics diagram in Figure 13, the trigger was vetoed if there was no beam, if the CAMAC registers were turned off, or if the computer was busy.

Outputs from the detectors were read out by computer automated measurement and control (CAMAC) and fast encoding readout ADC (FERA) modules into a μ VAX using the XSYS [17] data acquisition system. The data was then stored on compact discs for later analysis.

Chapter 3

ANALYSIS

3.1 Drift Chamber Analysis

The data analysis to this point has focused on calibrating the drift chambers and developing computer codes to determine the positions of charged particles as they passed through drift chambers.

3.2 Charged Particle Position in Drift Chamber

The first step in the analysis was to determine the location of charged particles that passed through the drift chamber. The procedure closely followed that described by Morris in Ref. [16].

As seen in Figure 14, the positions of particles as they pass through the drift chamber is the distance from the center of the chamber to the anode wire closest to the event plus or minus the drift distance of the ionization electrons as they move toward that anode wire. Thus, in order to determine the location of events in the drift chambers, it was necessary to know:

- 1) the anode wire to which the event was closest.
- 2) the drift distance of the ionization electrons from the event.
- 3) on which side of the nearest anode wire an event occurred.

The following discussion will describe how each of these quantities were determined.

3.2.1 Anode Wire Position

The first step in calculating the event position was to determine the anode wire nearest to the event.

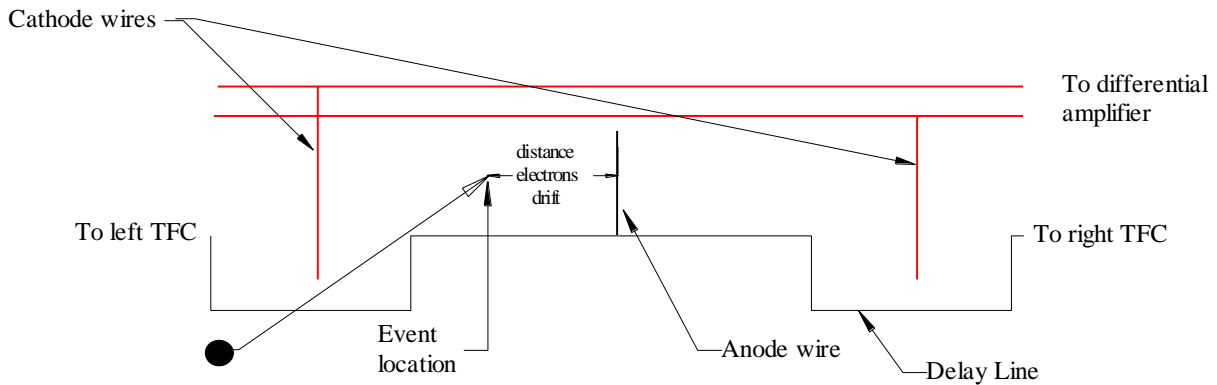


Figure 14. Schematic diagram showing a charged particle passing through a drift chamber plane. The location of the event in the drift chamber is equal to the location of the anode wire nearest to the event plus or minus the distance that the electrons had to drift to reach the anode wire.

As seen in Figure 15, the distance that signals from each anode wire must travel in both directions along the delay line to reach the TFCs is different depending on which anode wire the event was nearest.

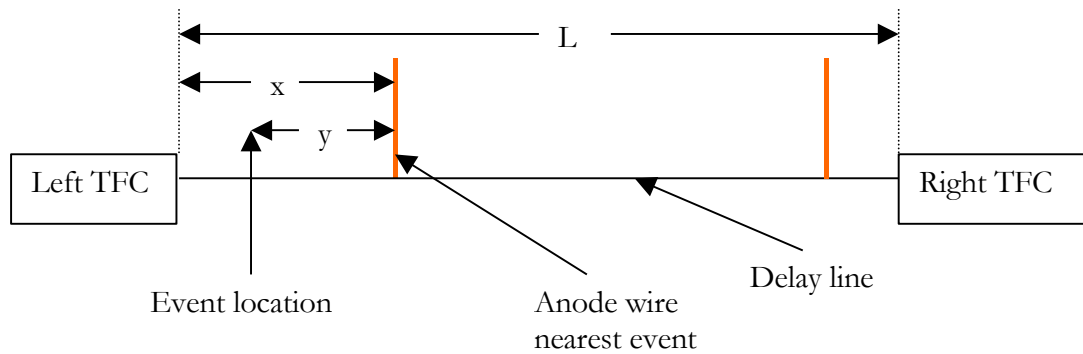


Figure 15. Schematic diagram illustrating the difference in path length for signals traveling along the delay line to the TFCs. L is the total length of the delay line, x is the distance that a signal coming from the anode wire nearest an event would travel to reach the left TFC and $L-x$ is the distance that a signal would have to travel to reach the right TFC. The distance that the electrons traveled to reach the nearest anode wire is y .

Since the delay line lengths traveled are different, the TFC times are also different. The time to reach the left TFC is

$$t_1 = \frac{x}{c} + \frac{y}{c'} \quad 3.1$$

where c is the velocity of the pulse and c' is the drift velocity of the electrons. The time to reach the right TFC is

$$t_2 = \frac{L-x}{c} + \frac{y}{c'}. \quad 3.2$$

The time difference between the arrival of the signals in the left TFC and the right TFC is then

$$t_d = t_2 - t_1 = \frac{L-x}{c} + \frac{y}{c'} - \frac{x}{c} - \frac{y}{c'} = \frac{L-2x}{c}. \quad 3.3$$

To find the location of the wire in terms of the time difference, Eq. 3.3 was solved for x ,

$$x = \frac{c}{2} t_d + \frac{L}{2}. \quad 3.4$$

Including a quadratic term to account for dispersion affects due to a long delay line [16], the event location in terms of the time difference between the left and right TFCs is

$$x = a_0 + a_1 t_d + a_2 t_d^2 \quad 3.5$$

where a_0 , a_1 , and a_2 are constants. To use t_d to determine the location of the wire nearest to an event, these constants must be determined. This was done by minimizing the chi-squared function,

$$\chi^2 = \sum_{i=1}^n (x_i - k_i)^2. \quad 3.6$$

This minimized the sum of the squared differences between the locations of anode wires nearest to events and the wire locations given by

$$k = \text{Int}(x/w)w \tag{3.7}$$

where Int is a function that truncates its argument to the nearest integer and w is the known spacing between anode wires, 8 mm. Figure 16 shows a histogram for a drift chamber x-plane where the light gray peaks are the events closest to different anode wires, as determined by Eq. 3.5 and the black lines are the locations of the anode wires in the drift chamber as determined by Eq. 3.7

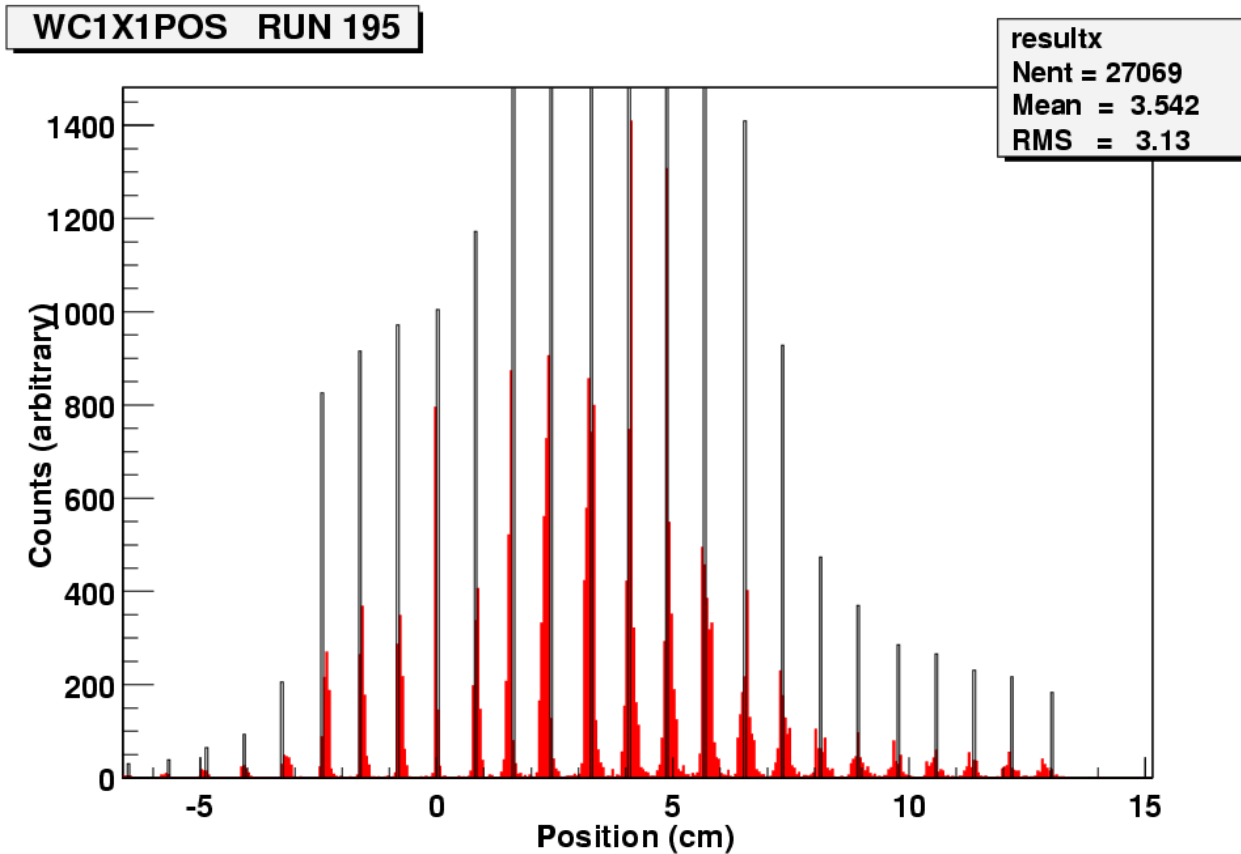


Figure 16. Typical histogram of wire position. The gray peaks correspond to the positions of events in the chamber as given by Eq. 3.5 and the black to the location of wires in the chamber as determined by Eq. 3.7.

3.2.2 Electron Drift Distance

Once the location of the nearest anode wire had been determined, the next step was to find the distance that the electrons drifted from the event location to the nearest anode wire. As discussed in Section 3.2.1, the time it takes for a signal from an anode wire to reach each end of the delay line is different. It is also necessary to consider the drift time which is defined to be the time that it takes for the electrons from the event to drift to the anode wire. The drift time is given by

$$t_{\text{dr}} = \frac{y}{c'} \quad 3.8$$

where t_{dr} is the drift time, c' is the drift velocity of the electrons, and y is the distance from the event location to the nearest anode wire, as shown in Figure 15. To determine the drift time in terms of the known times for a signal to travel from the anode wire to each TFC, find the total amount of time that it took from when the event occurred to when the signals reached the TFCs,

$$t_s = t_1 + t_2 = \frac{x}{c} + \frac{y}{c'} + \frac{L-x}{c} + \frac{y}{c'} = 2t_{\text{dr}} + \frac{L}{c}. \quad 3.9$$

Solving Eq. 3.9 for the drift time,

$$t_{\text{dr}} = \frac{1}{2} \left(t_s - \frac{L}{c} \right). \quad 3.10$$

Thus the drift time is related to the sum of the times from the TFCs by a constant (path length correction). Assuming that the drift chambers are evenly illuminated by charged particles from the target, the distribution of charged particles in drift time (dN/dt) should be related to the distribution of charged particles in space (dN/ds) as shown in Eq. 3.11. The drift velocity of the electrons is ds/dt and A is a constant for even illumination of the chamber, so

$$\frac{dN}{dt} = \frac{dN}{ds} \frac{ds}{dt} = A \frac{ds}{dt}. \quad 3.11$$

To find the drift distance as a function of drift time, $s(t)$, it is necessary to integrate the distribution of charged particles per time with respect to drift time,

$$s(t) = \frac{1}{A} \int_0^t \left(\frac{dN}{dt} \right) dt. \quad 3.12$$

After integrating the charge distribution in time with respect to time, the constant A must be determined.

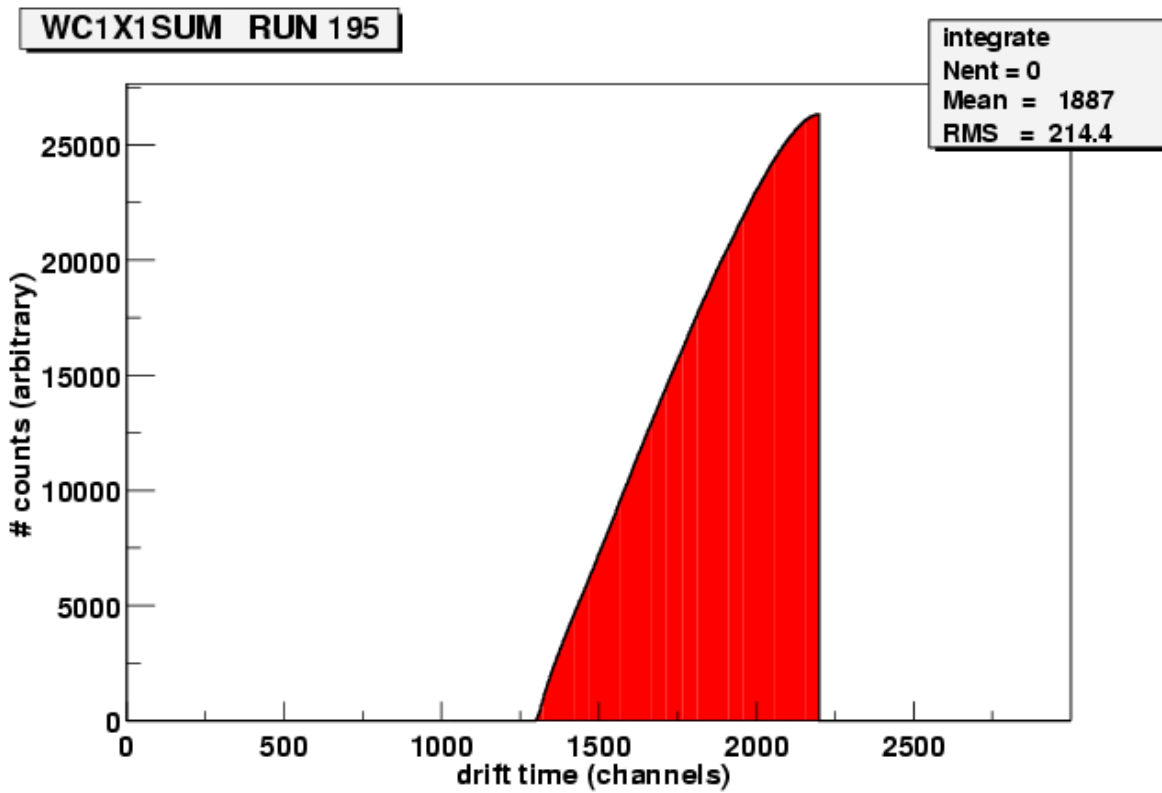


Figure 17. Plot of integrated counts per time. Notice the sharp cut off just before channel 2250, which corresponds to the maximum drift time and thus the maximum drift distance of 4 mm.

Figure 17 shows a plot of the integrated counts with respect to time for the x-plane of one of the drift chambers. The sharp cut-off to the right corresponds to the longest drift time possible and the cut-off to the left corresponds to a drift time of 0 seconds. The longest drift time should come with the greatest drift distance, which is half the distance between two anode wires (4 mm) so A may be determined. Once A has been determined, the plots of integrated counts versus drift time may be used to find the drift distance for any given drift time.

3.2.3 Cathode Pulses

The final step to determine where in the drift chamber the event occurred was to decide on which side of the anode wire an event occurred. The output from the differential amplifier shown in Figure 12 was either positive or negative depending on which cathode wire was closer to the event. The output from the analog to digital converter (ADC) shows two peaks, as in Figure 18.

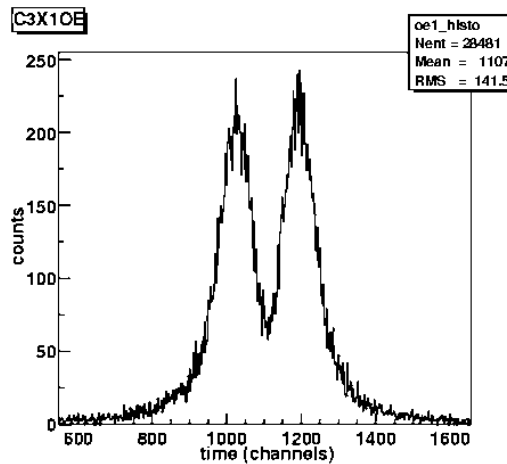


Figure 18. Histogram of the output from the ADC. The left and right peaks correspond to events occurring on either side of the anode wire and the center valley corresponds to events close to the anode wire so that pulses in the cathode wires on either side are about the same size.

As illustrated in Figure 19, one peak corresponded to events occurring nearest an odd cathode wire. The other peak corresponded to events occurring nearest an even cathode wire. The decision to either

add or subtract the drift distance from the anode wire position depended on the anode wire. In Figure 19, the drift distance may be added to the anode wire to the left of the odd cathode wire. Then the drift distance will be subtracted from the anode wire to the right of the odd cathode wire. Similarly, the drift distance will be added to the anode wire to the left of the even cathode wire, but subtracted from the anode wire to the right of the even cathode wire. Thus it was only necessary to determine whether the drift distance is added or subtracted from the first anode wire.

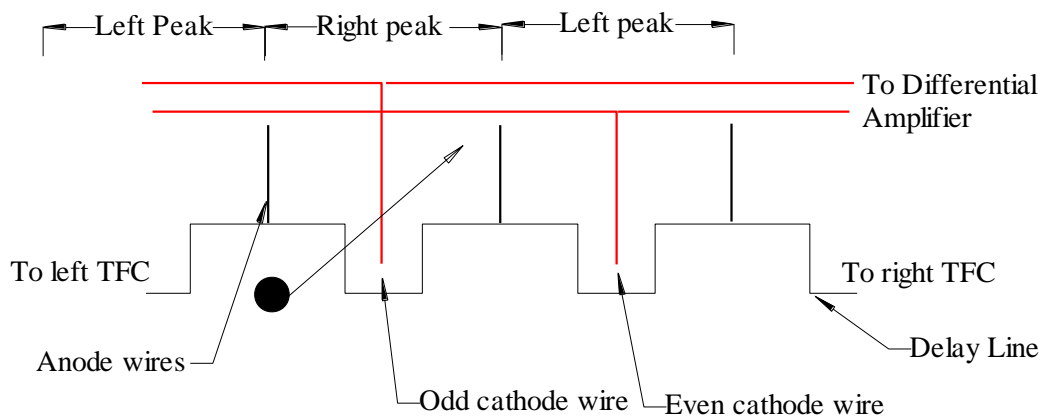


Figure 19. Schematic diagram of a charged particle passing through a drift chamber plane. The events closest an odd cathode wire will correspond to one peak in Figure 18 while events that occur closest to an even cathode wire will correspond to the other peak.

Notice that the valley in the middle of Figure 18 corresponded to events that occurred so close to the anode wire that the pulses in the cathode wires to either side of the event were about the same size.

To determine whether to add or subtract the drift distance from the first anode wire, it was necessary to decide which peak corresponded to adding the drift distance and which corresponded to subtracting the drift distance for a given wire. To determine this, the track position in a drift chamber was plotted against the track position in the drift chamber directly behind it. For the correct choice of adding and subtracting the drift distance, the plot was a smooth distribution. In all other cases the distribution was jagged. The results for the x-plane of one of the drift chambers may be seen in Figure 20 where the correct decision for which peak corresponded to events that should have the drift distance added

to the closest wire and subtracted from the next closest is in the top left corner.

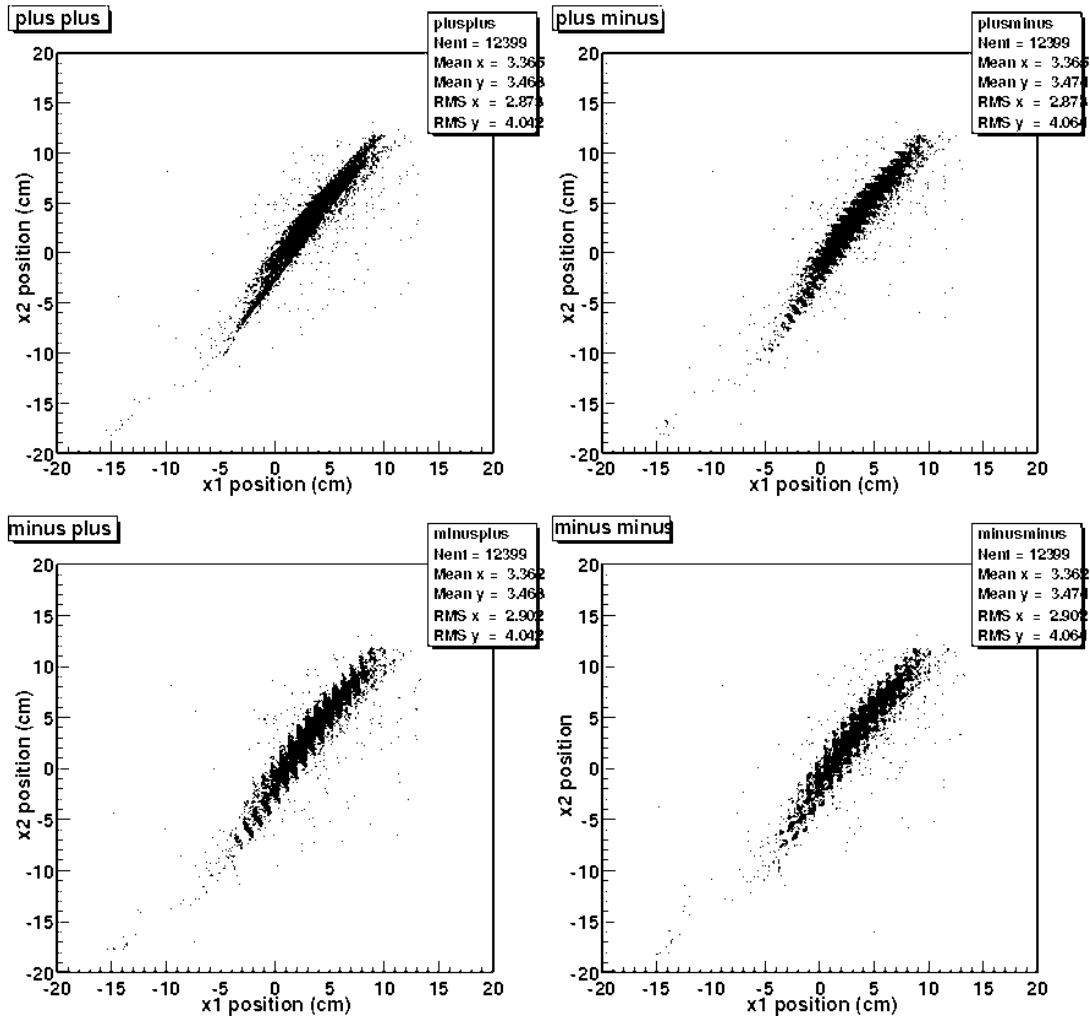


Figure 20. The four possible configurations for adding or subtracting drift distances. The correct configuration is the smooth distribution at the top left. The zeros shown on the plots are arbitrary.

3.3 Position with Respect to the Beam Line

After determining the location of events within the different drift chambers, the location of the events with respect to the beam line was determined. This was done by placing lead bricks in front of the

drift chambers at known positions, as shown in Figure 21.

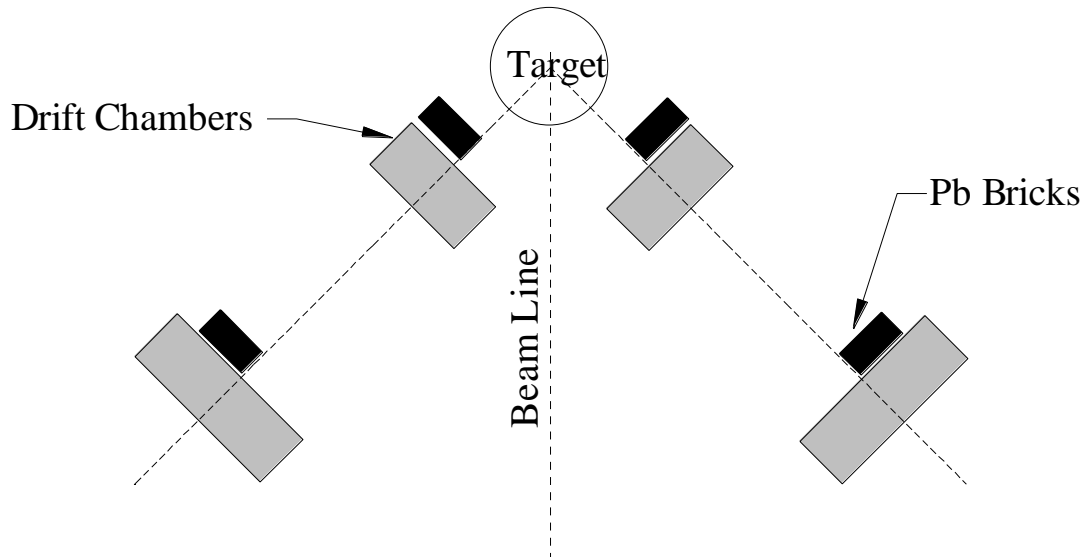


Figure 21. Schematic of the placement of the lead bricks in front of the drift chambers. The bricks were placed outside the center lines away from the beam line.

Many charged particles striking the lead bricks were stopped and thus did not enter the drift chambers. The locations of the bricks with respect to the beam line were measured. By plotting the x position versus the y position for each drift chamber, it was possible to determine the location of the bricks in front of the drift chambers since the density of events in that region was much less than elsewhere in the chamber. For the front set of drift chambers in the magnetic spectrometer to the left of the beam line, the lead brick covered the end of the drift chamber so plots of x versus y planes were cut off where the brick was in front of the chamber (see Figure 22). For the front set of drift chambers in the magnetic spectrometer to the right of the beam line and the back sets of drift chambers, there were regions of lesser density in the plots of x versus y corresponding to the brick in front of the chambers, as seen in Figure 22 and Figure 23. Notice also that in the rear chambers, the gaps between the plastic scintillators of the calorimeters are clearly visible in the plots of x versus y.

Once the locations of the bricks have been identified, it will be possible to determine the location of the bricks in relation to the beam line and then the location of events with respect to the beam line (see Appendix C).

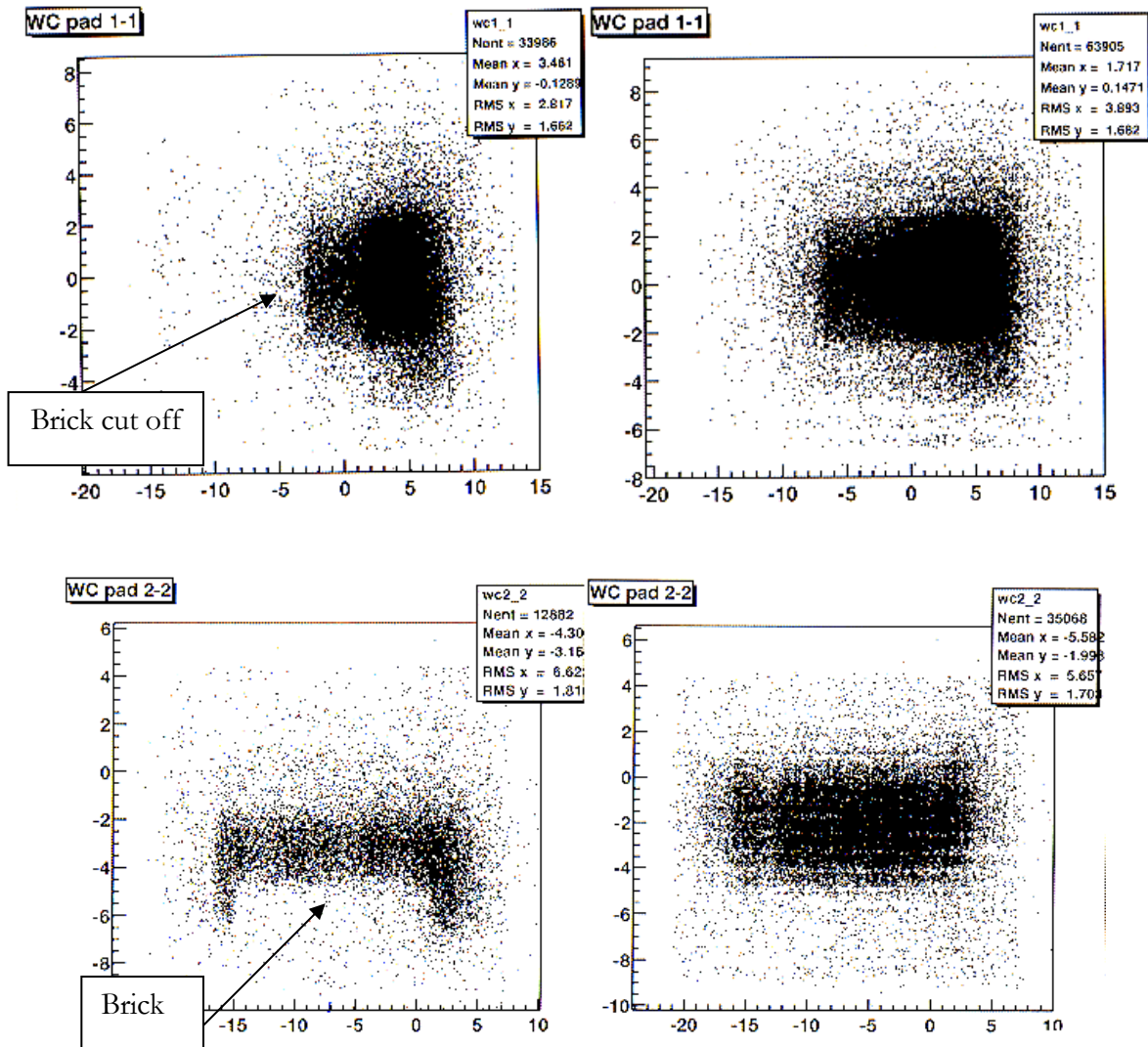


Figure 22. Plot of plane x versus plane y for the first drift chamber of the magnetic spectrometer to the left of the beam line (above) and to the right of the beam line (below). The plots at left have a brick over part of the drift chamber, the plots on the right do not. The dark regions seen are the ΔE detectors which are included in the event trigger.

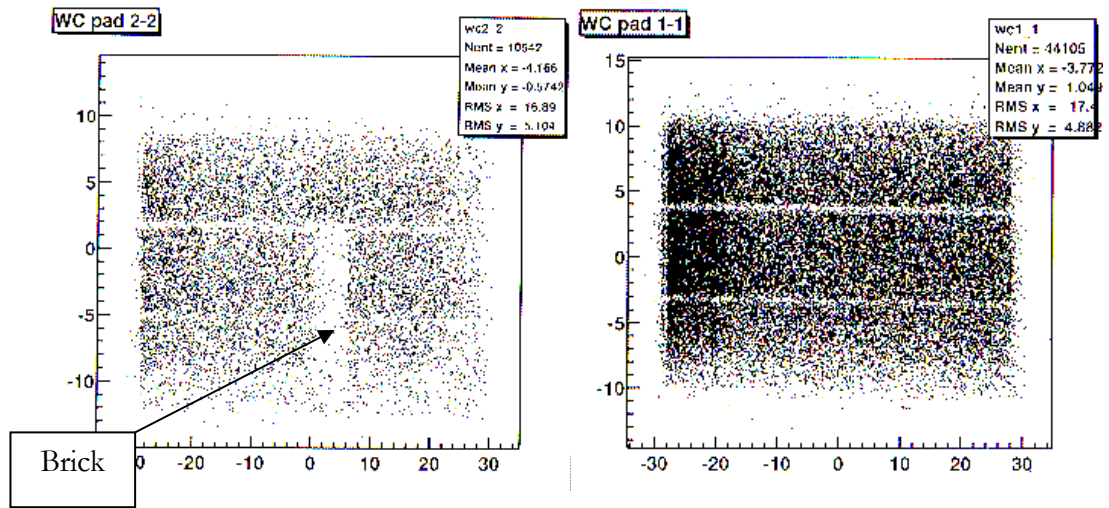
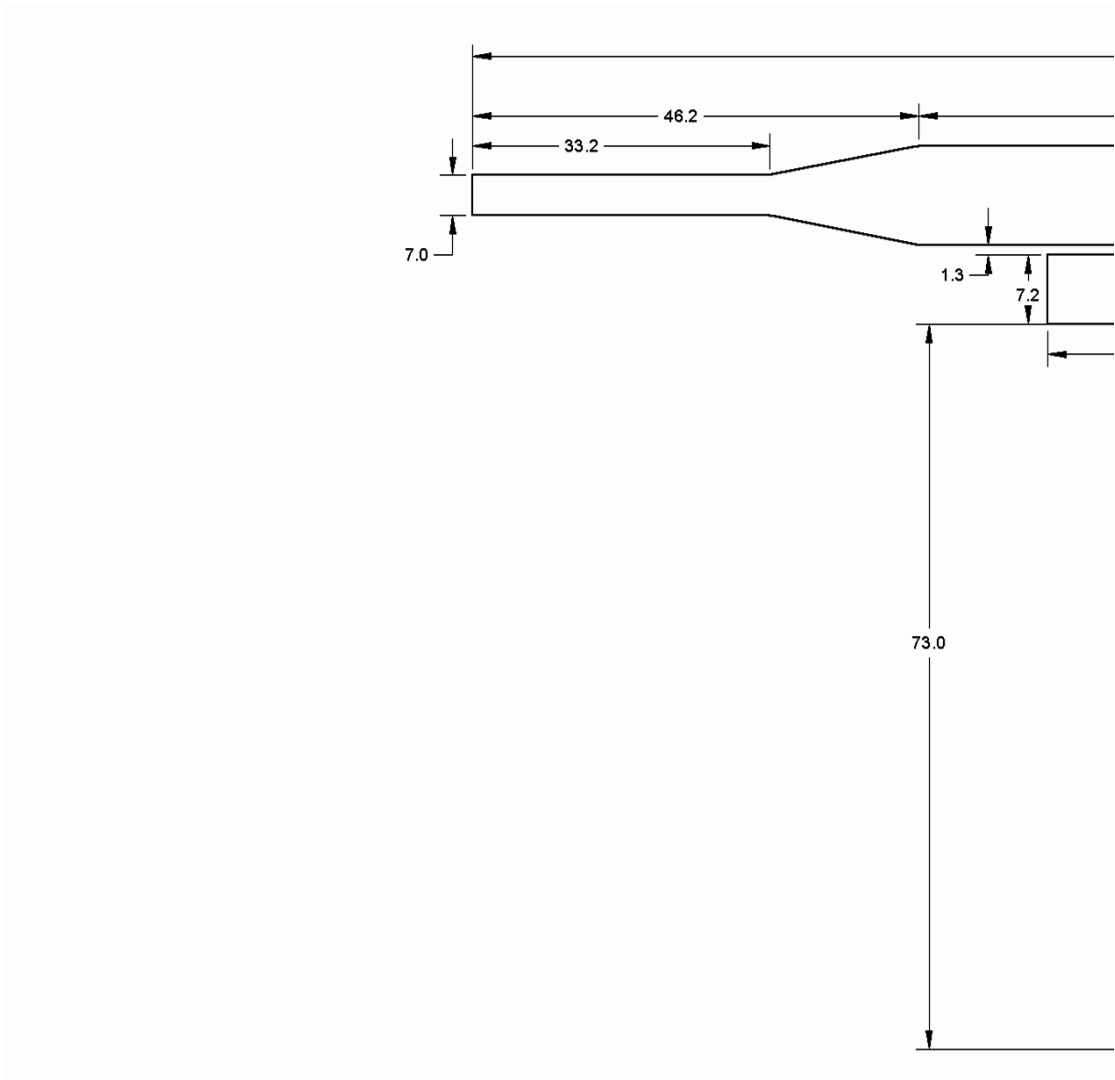


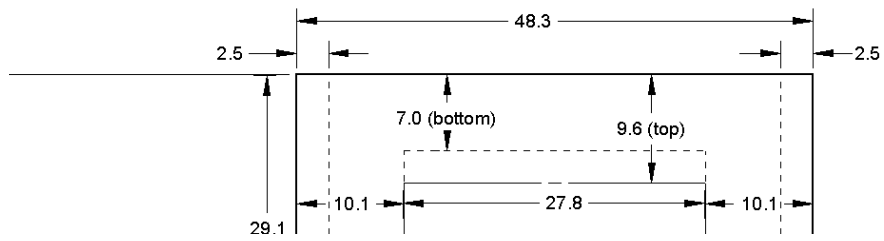
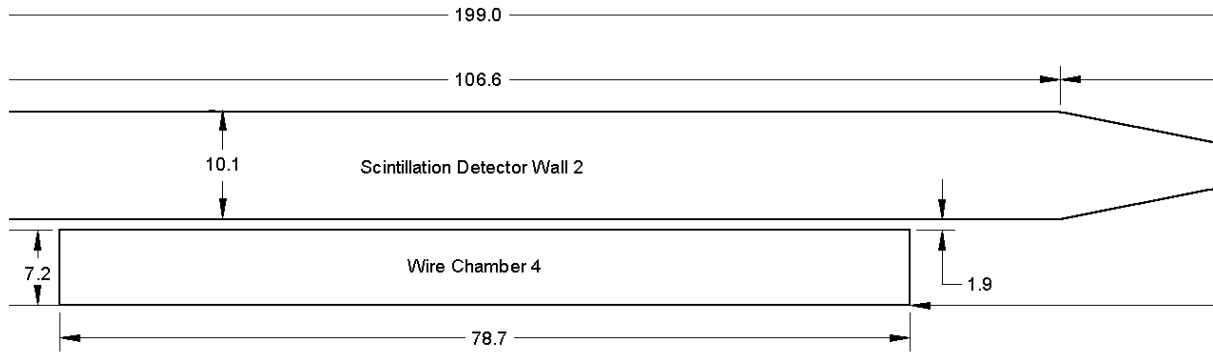
Figure 23. Plot of plane x versus plane y for the rearmost drift chamber of the magnetic spectrometer to the left of the beam line. The plot in the left has a brick over part of the drift chamber, the plot on the right does not. The two light regions seen in the plots are the gaps between the stacked scintillators of the calorimeter.

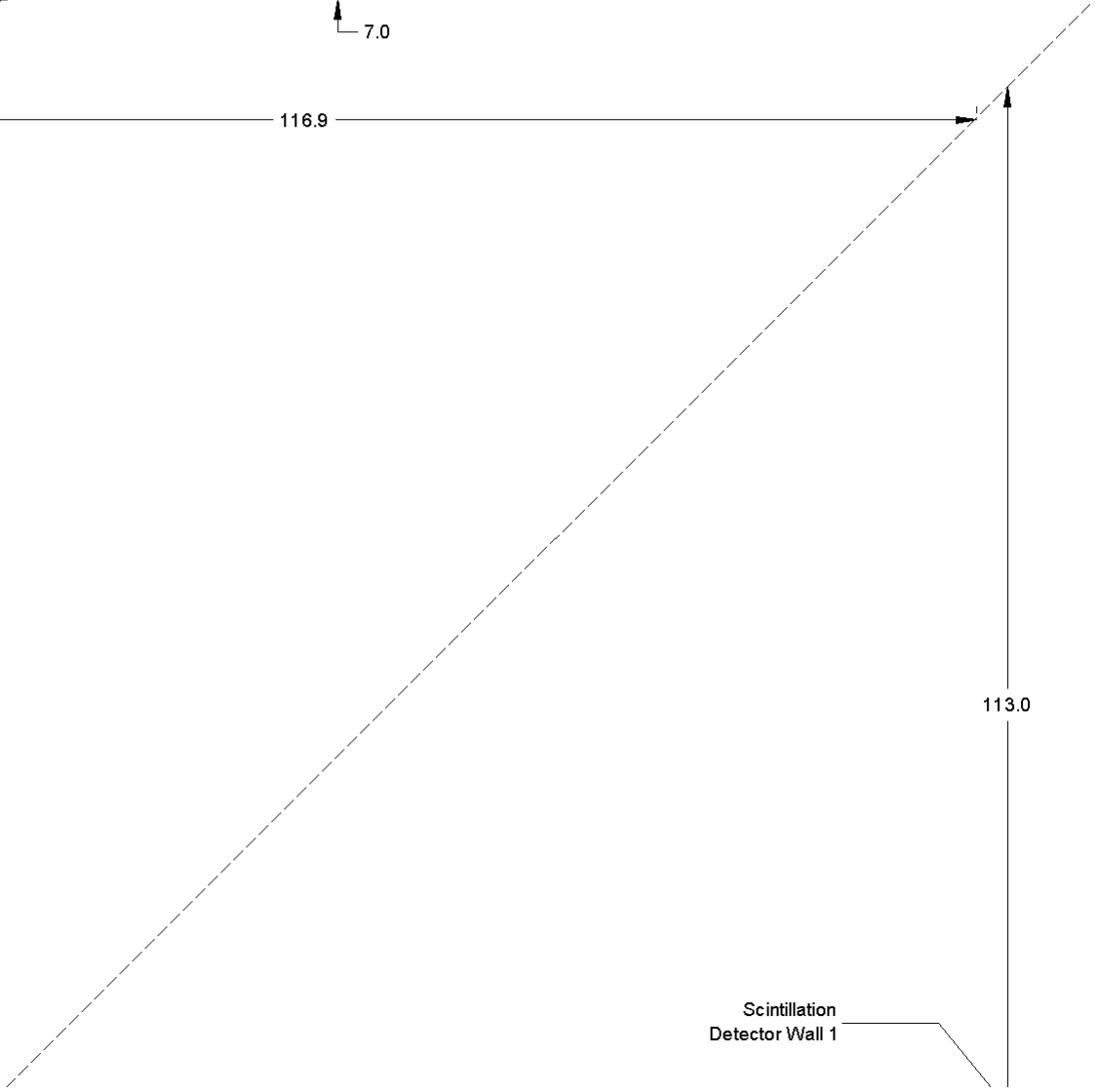
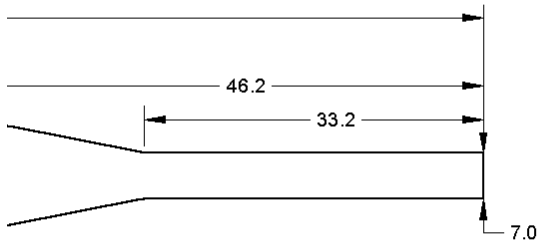
Chapter 4

CONCLUSIONS

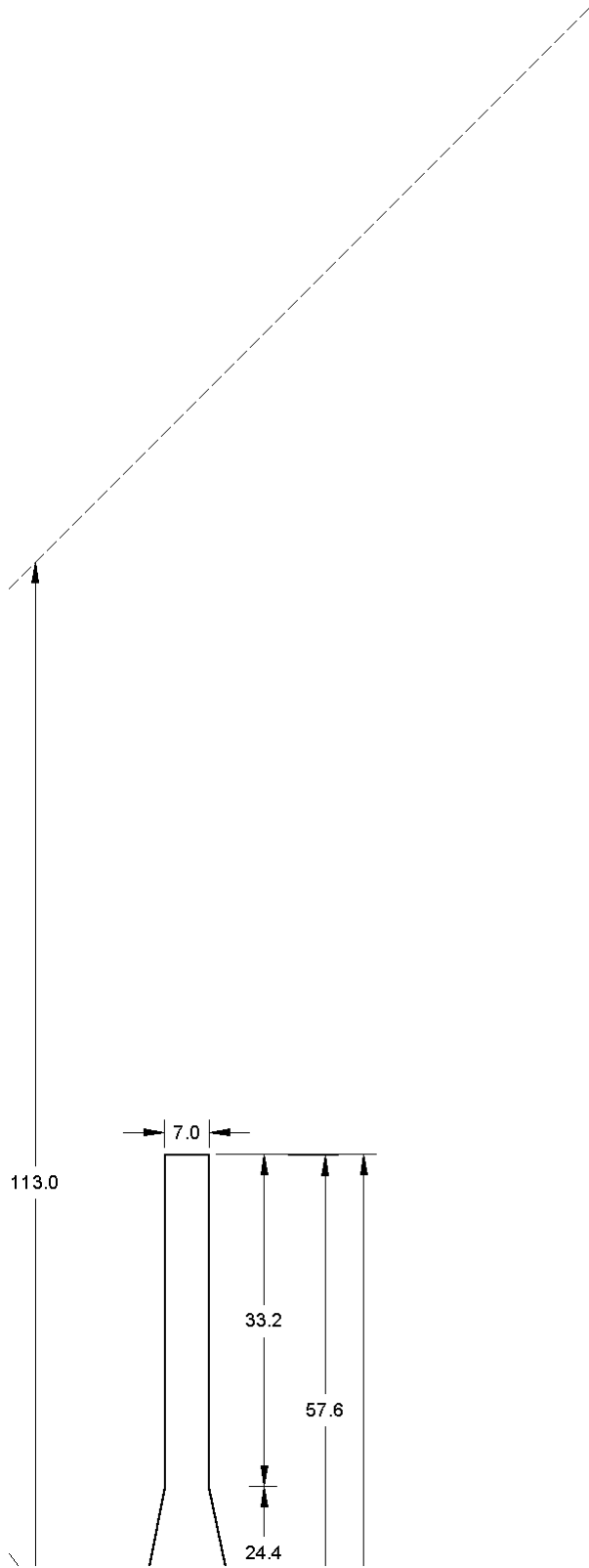
This experiment investigated the Δ^{++} component to the ${}^3\text{He}$ and ${}^4\text{He}$ nuclear wave function. The experiment was set up along the 90 meter FP15L at the WNR facility of LANSCE. An incident neutron beam interacted with the ${}^3\text{He}$ and ${}^4\text{He}$ targets and outgoing protons were detected in magnetic spectrometers 45° to the left and right of the beam line. Analysis has focused on determining the location of charged particles as they pass through the drift chambers. The location of events within the drift chambers has been determined and currently the locations of events with respect to the beam line are being calculated. The locations of events as they pass through the sets of drift chambers provide the two points from which the trajectories of the particles before and after the permanent magnet may be determined. When the charged particles passed through the magnetic fields of the permanent magnet, their trajectories were deflected. Once the locations of events in the drift chambers have been found, the changes in trajectory may be calculated. From the changes in trajectory, the momenta may be determined and once the momenta have been determined, the differential cross section of the Δ^{++} component to the ${}^3\text{He}$ and ${}^4\text{He}$ may be calculated.

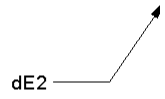
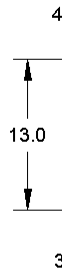




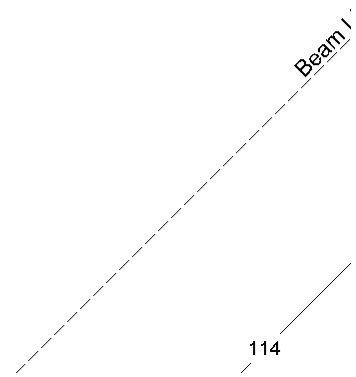


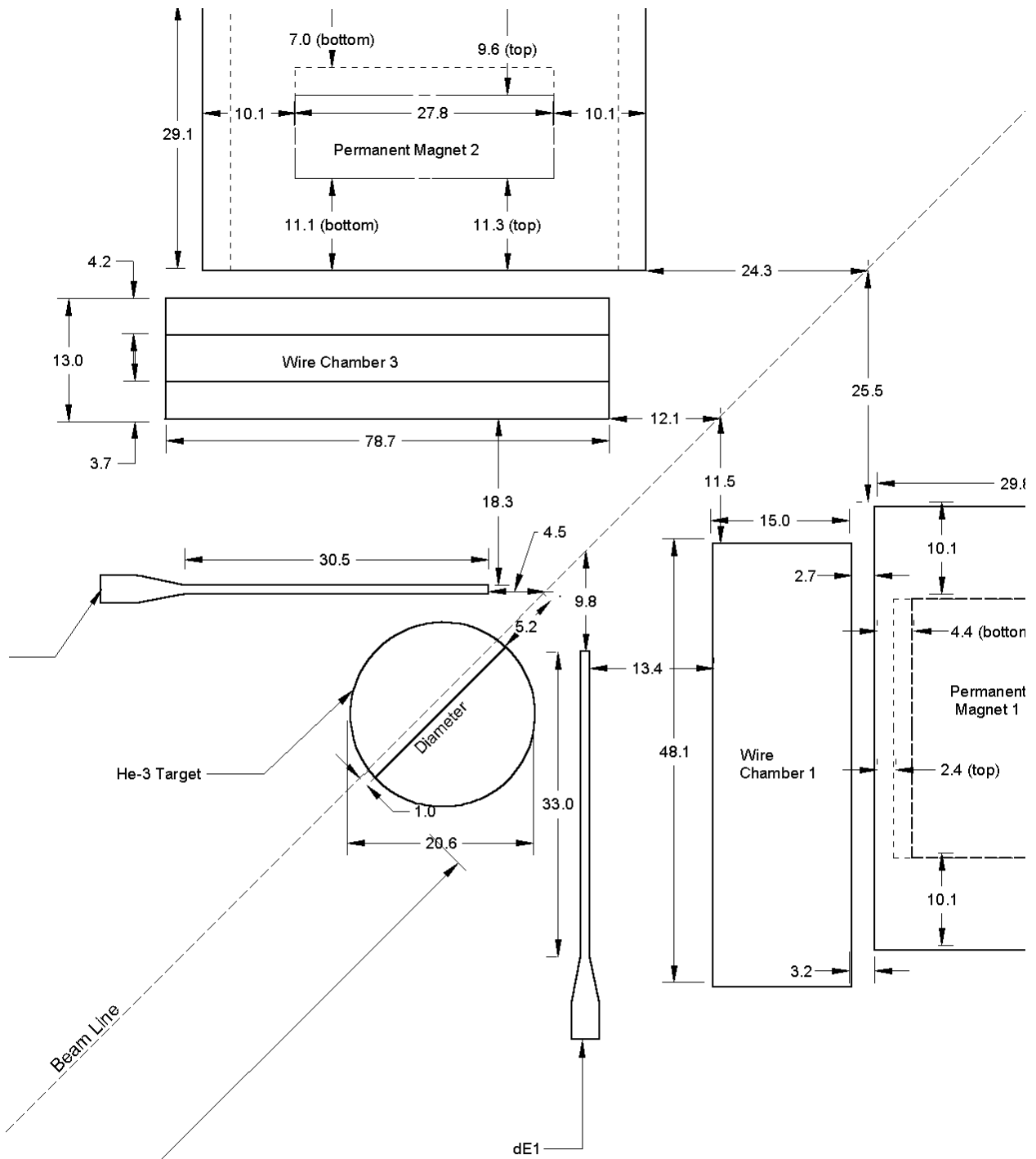
Scintillation
Detector Wall 1

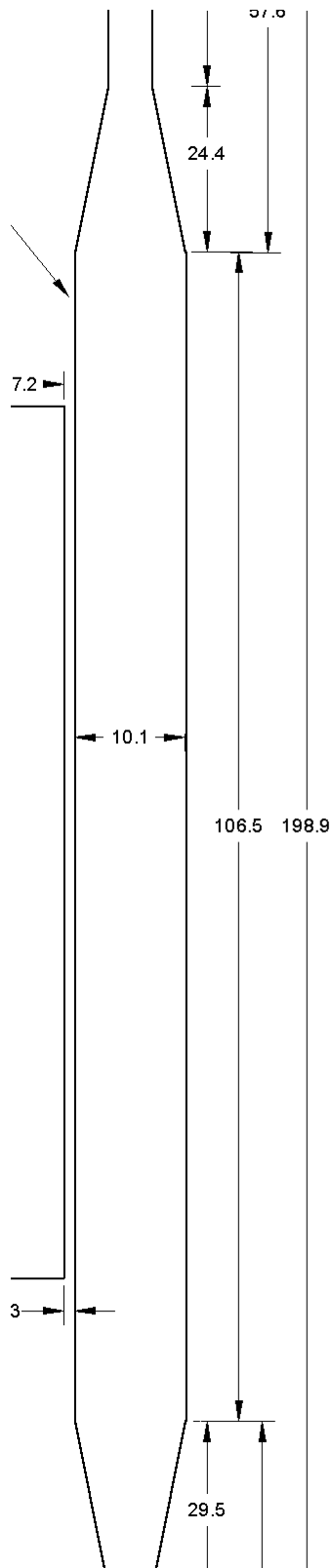


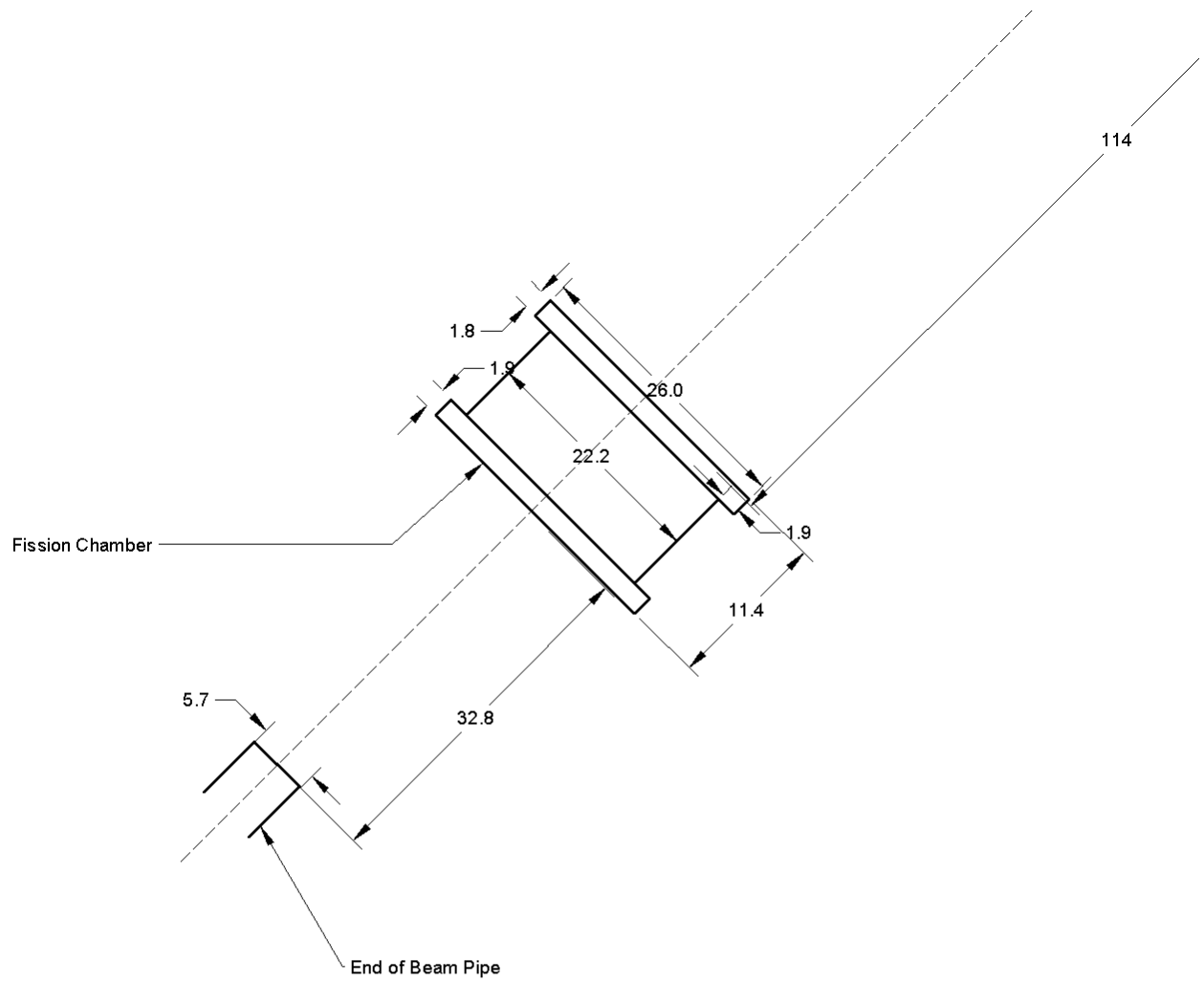


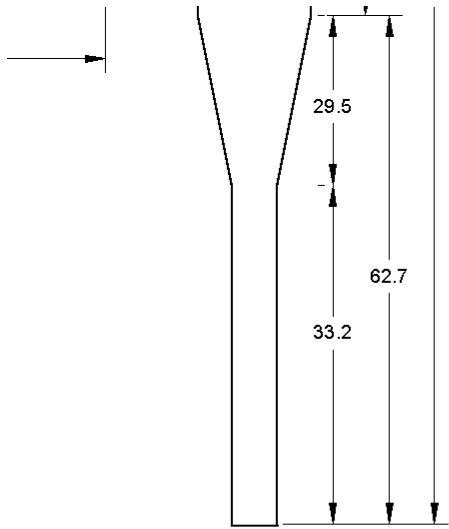
44











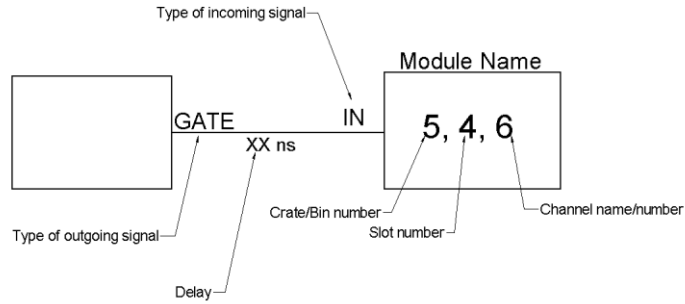
David Constantine
Sara Mahoney
Willi Suckau
Jeremy Vecchi
(n,2p) Geometry
7/21/00

Appendix B

COMPLETE ELECTRONICS SCHEMATICS

The following electronics diagrams show the complete trigger electronics and the FERA modules for the drift chambers. The format for giving the bin and crate number is explained in the legend.

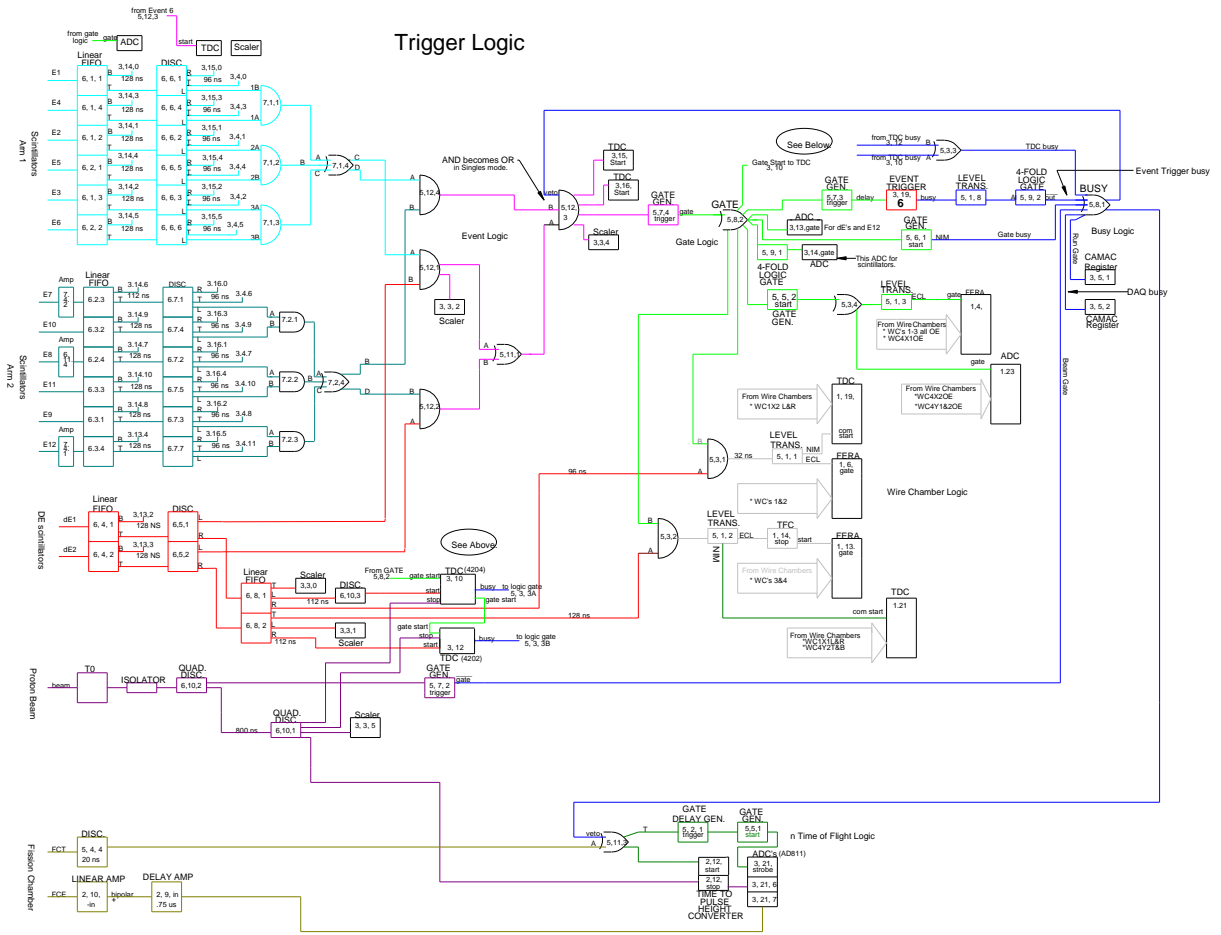
Electronics Legend (n, 2p)

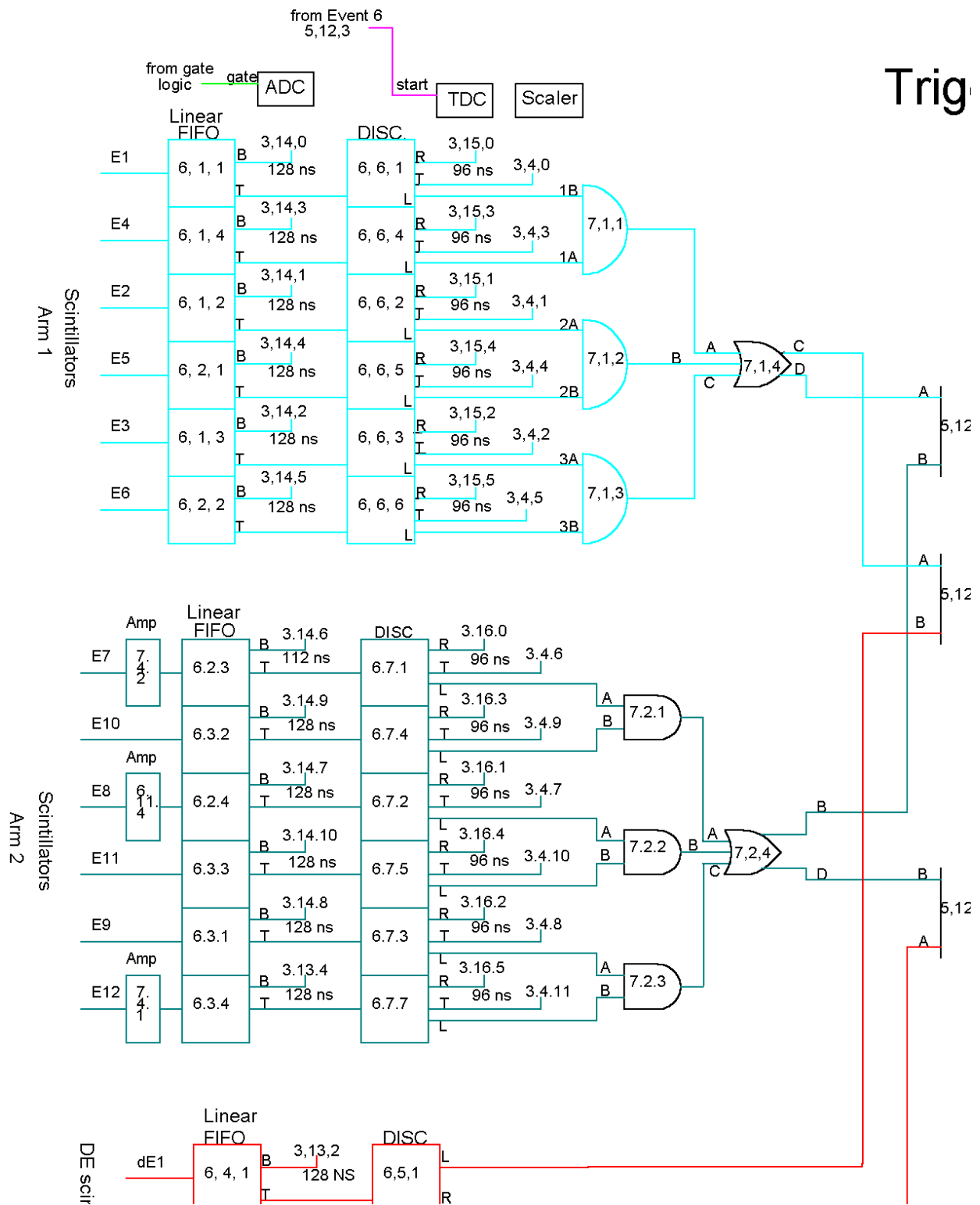


Crate/Bin Setup

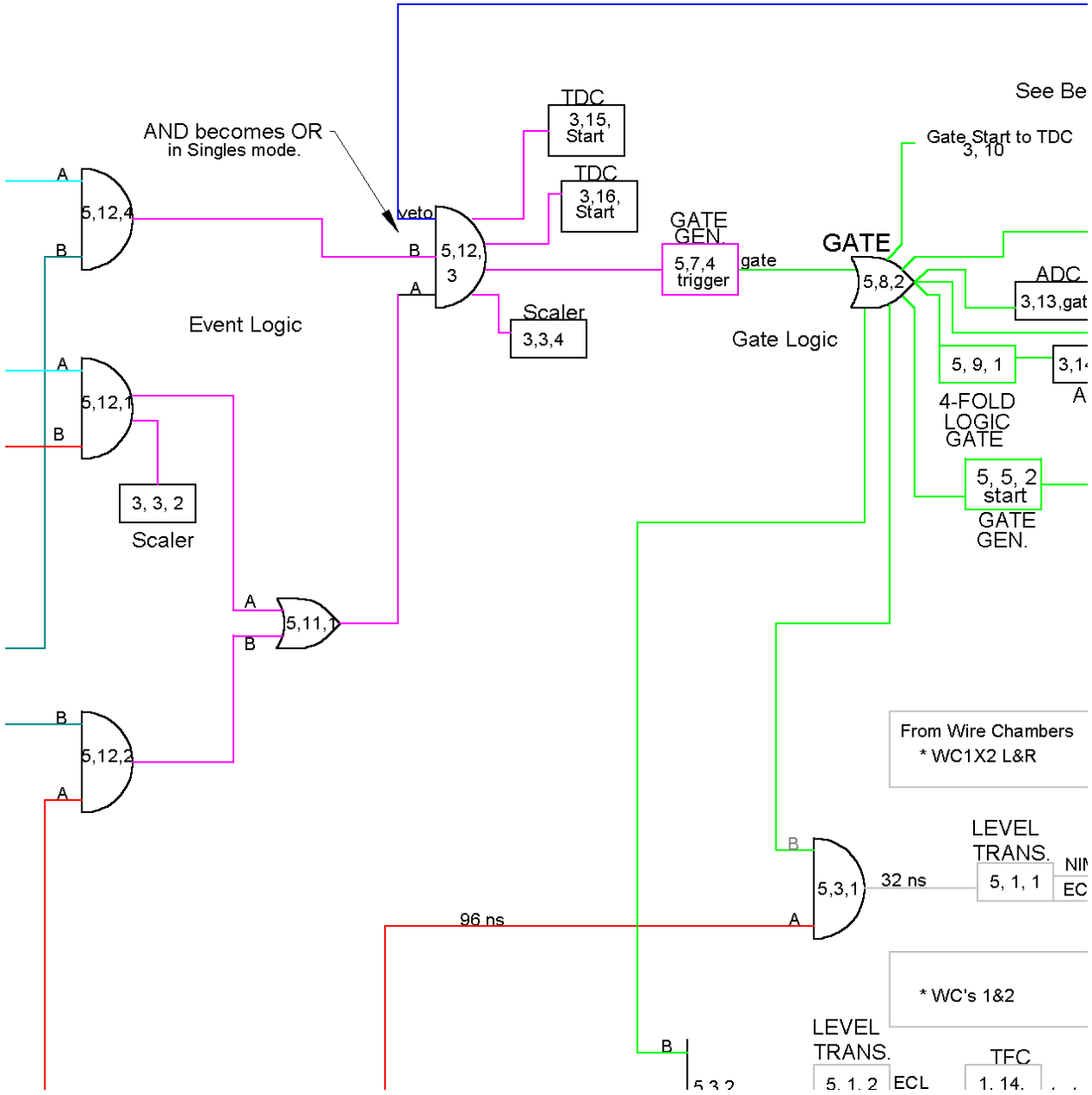
1. CAMAC Crate	3. CAMAC Crate	
2. Bin	4. Bin	Oscilloscope
Delay	5. Bin	6. Bin
Incoming Signals		Delay
Incoming Signals		Delay

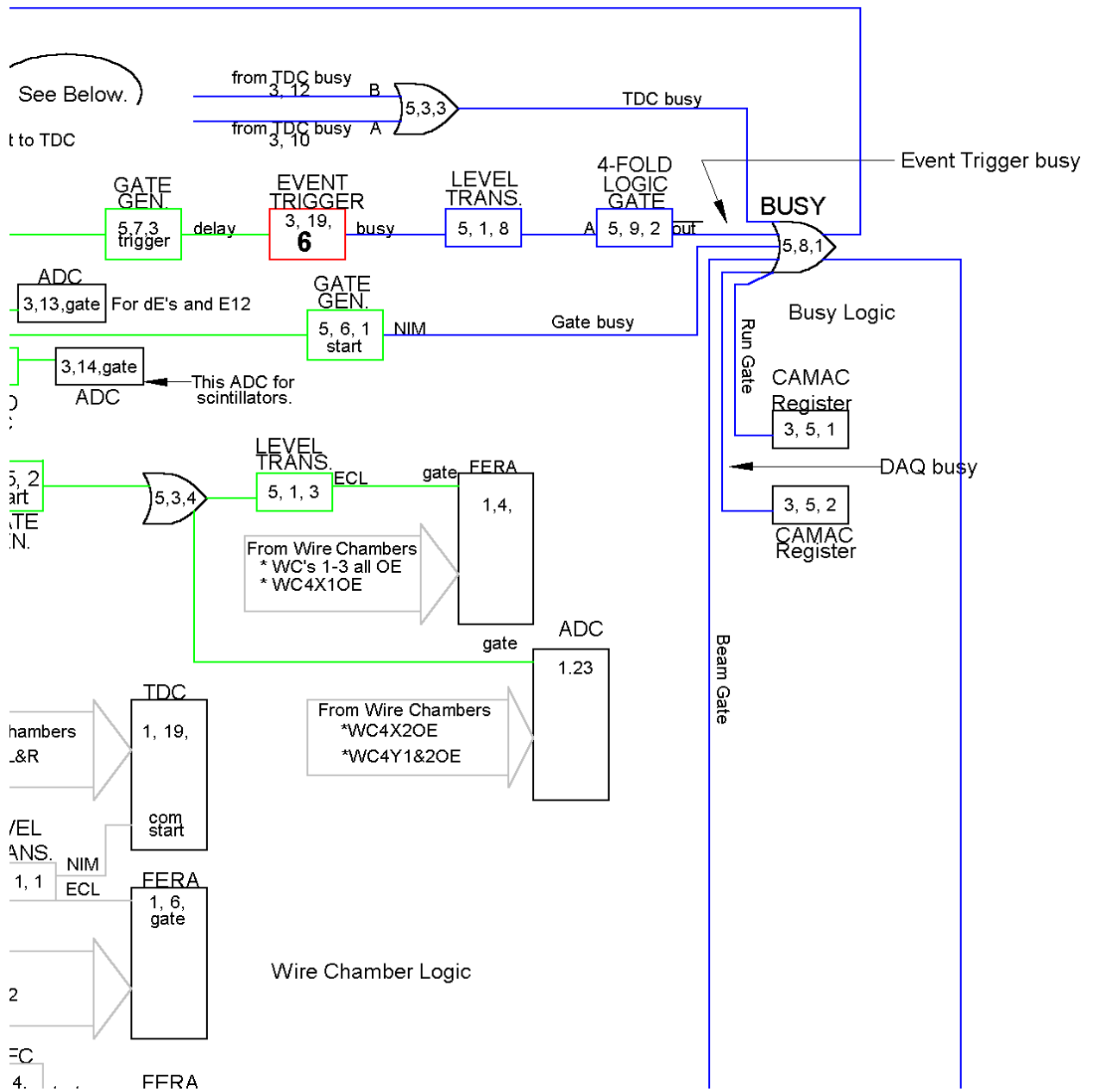
Trigger Logic

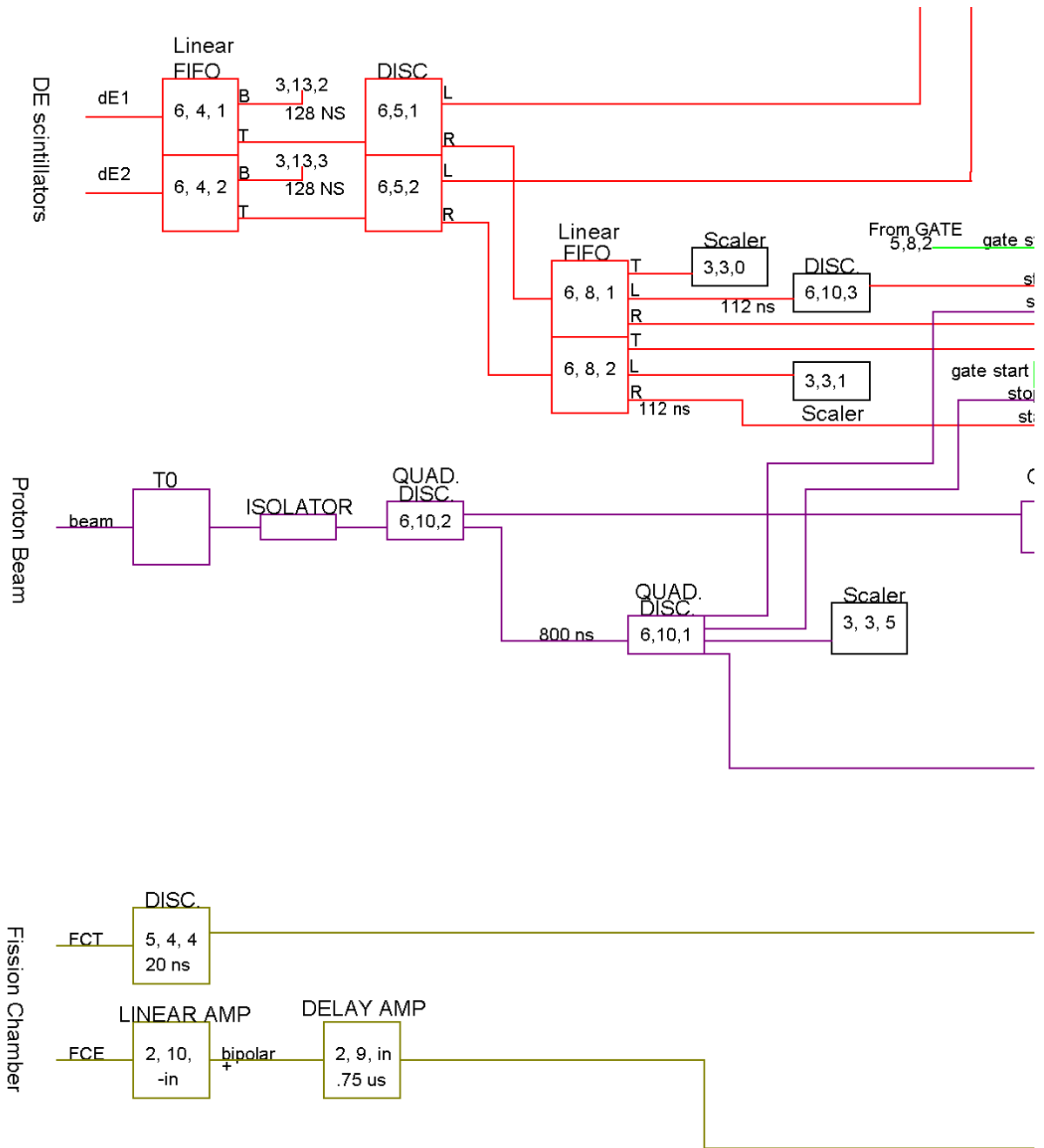


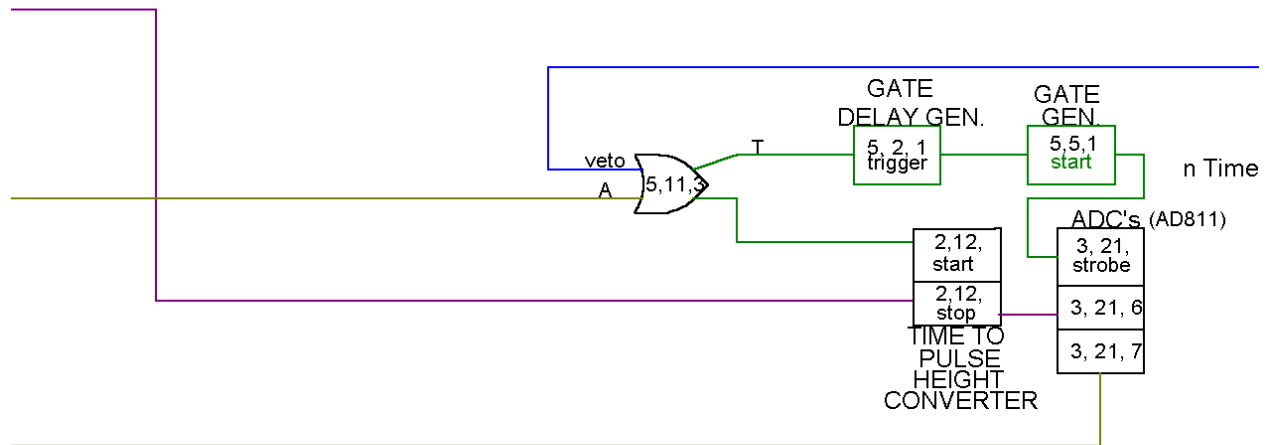
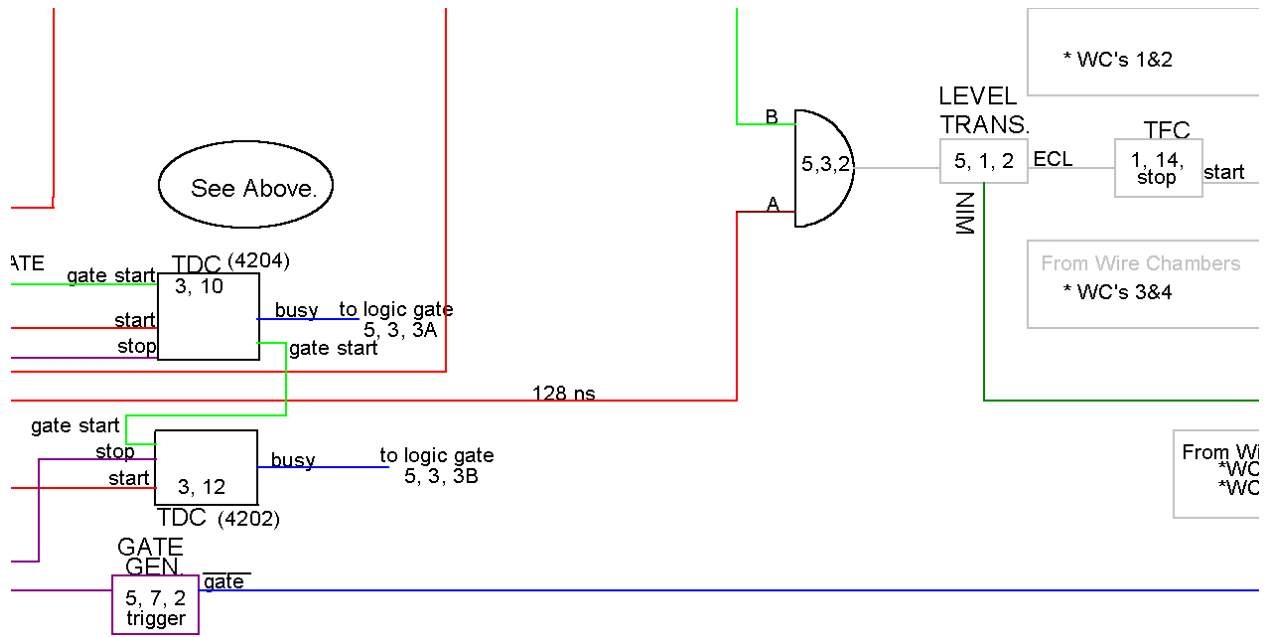


Trigger Logic

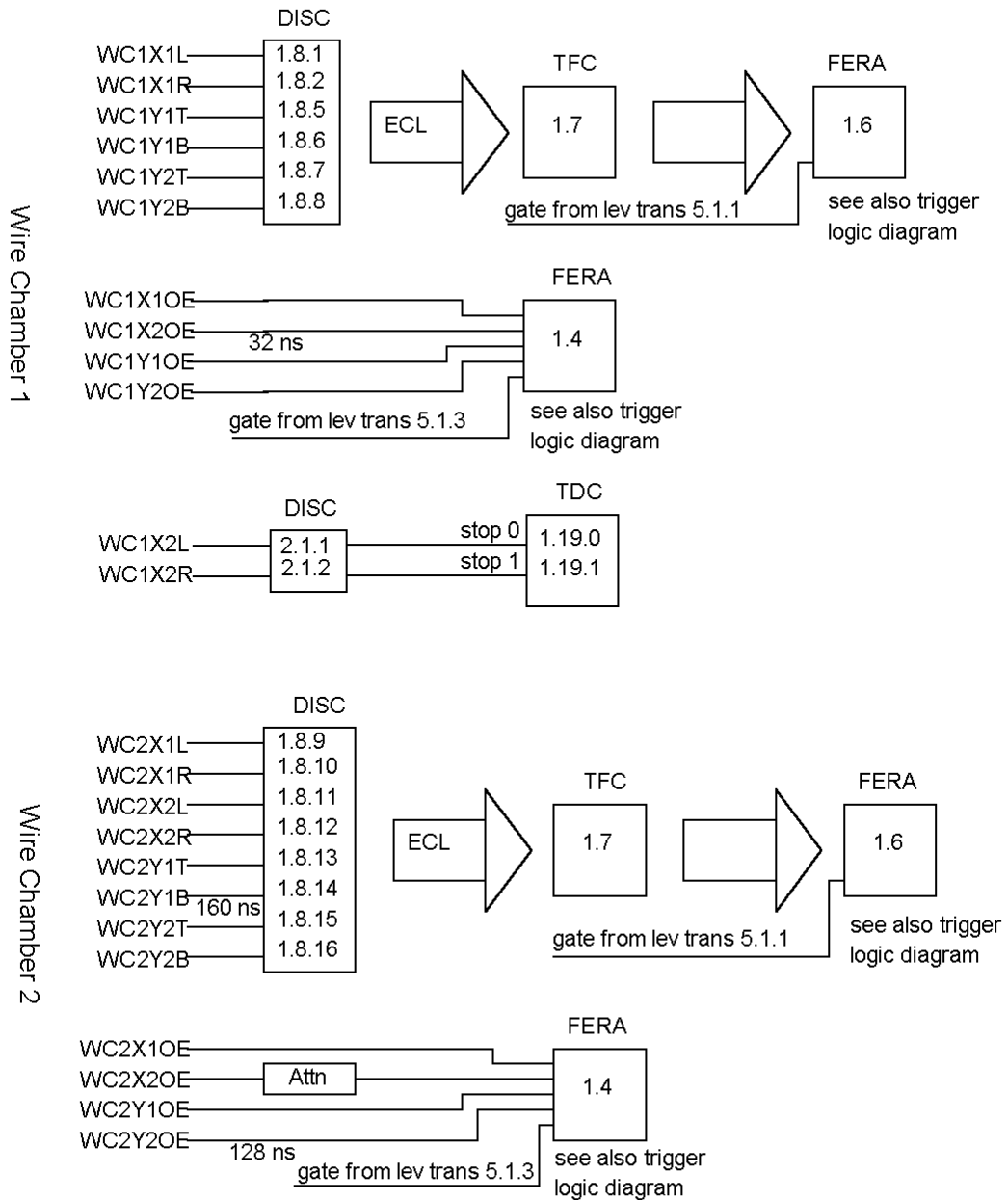


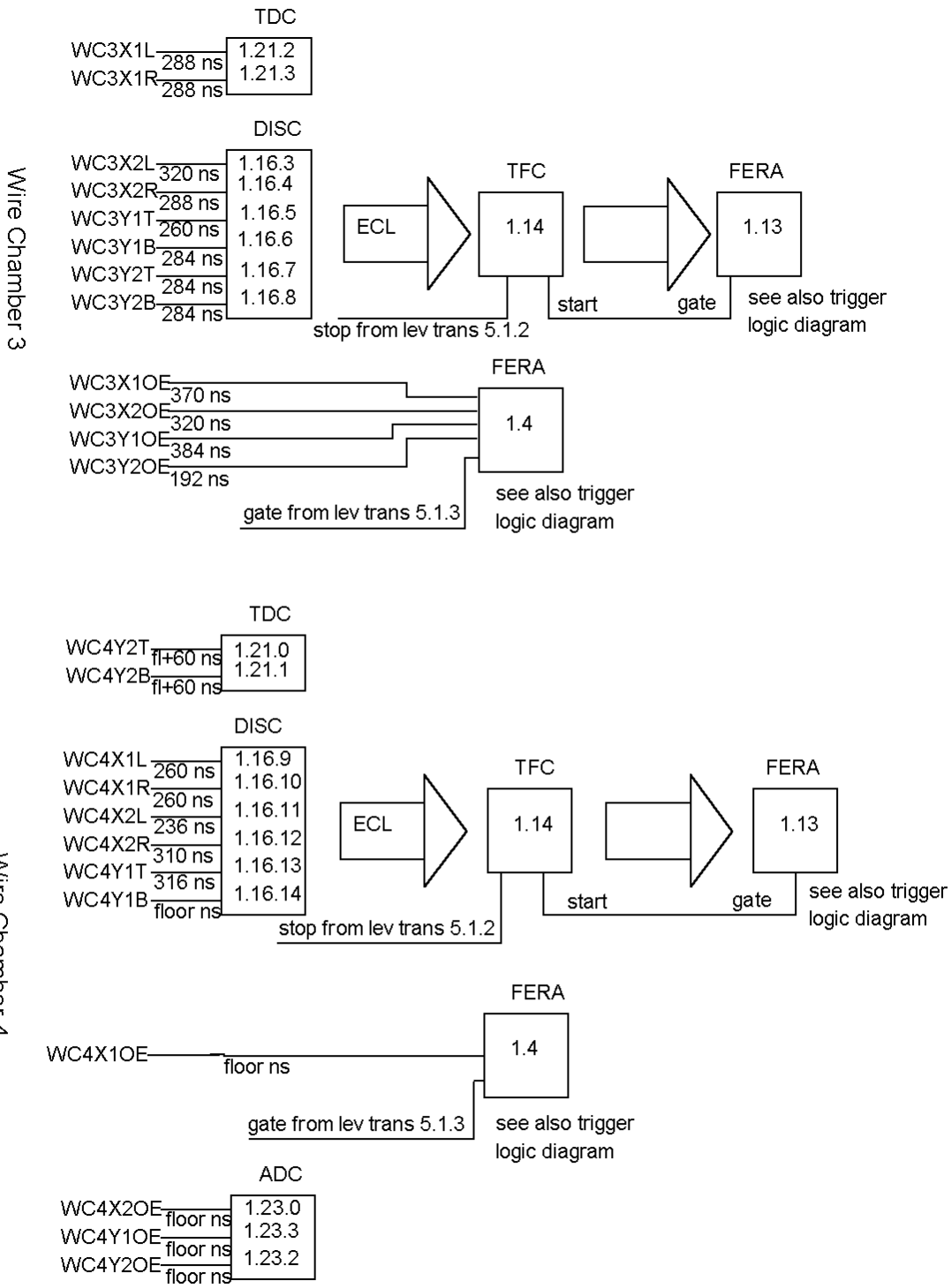






Wire Chamber Logic





Appendix C

DESCRIPTION OF COMPUTER CODES

C.1 Overview

Computer codes were developed to analyze the readouts from the drift chamber TFCs to determine the location of events in the drift chambers. Since the data were originally stored in an XSYS [17] format, a C++ code was developed to convert from the XSYS (.evt) format to a ROOT (.root) format so that the ROOT [18] interactive data analysis framework could be used for the analysis. Once that was completed, ROOT macros were written to carry out the data analysis steps described in Chapter 3.

C.2 Conversion from XSYS to ROOT

The code that converted the data from XSYS format to ROOT format was called `evt2root.C` and saved the individual readouts from the FERA and CAMAC modules into branches and leaves of a ROOT tree. The code accepted as the XSYS file name as the input parameter. The code then read in the raw data to a ROOT tree. A ROOT class event containing data from the FERA and CAMAC modules was stored as a branch on the tree. A new class called `Evio` was used to read in the data elements from the XSYS format. Since there were changes in the FERA module inputs during the course of the experiment, `evt2root.C` used the run number to determine which leaf to save the FERA outputs to.

C.3 Determining Event Position Within Drift Chamber

Codes were developed to determine the coefficients for Eq. 3.5 (relating the time difference between the left and right TFCs to the position of events in the drift chamber), find the constant in Eq. 3.12 (relating the drift time to the drift distance), and determine whether to add or subtract the drift distance to anode wires. ROOT trees containing the data were saved to the `/delta00/data` directory by a ROOT macro called `evt2root_all.C` which ran `evt2root.C` on each of the XSYS data files. The

ROOT trees were saved using the format “deltaX.root” where X was the run number. Macros were saved in /delta00/macros, and logs of the commentaries from the running of each macro were saved in /delta00/logfiles using the same format as for the data files except that the file extension was .log. The output files from each macro were saved in /delta00/database.

C.3.1 Cuts Applied During Analysis

To eliminate background and some noise at the beginning of each run, cuts were made to select out channels of greatest interest for analysis. Histograms of the raw data were used to determine cuts for the run being used for calibration, Run 195. This run was with a hydrogen target and in singles mode so that the event trigger did not require coincidence signals from the left and right TFCs. The cuts were saved to a text file called deltatests_cuts.txt in the /delta00/database directory. This was the default cut file and was accessed and applied by each ROOT macro used in the analysis. Cuts could be determined for each run in this manner and would be named deltatest_X.txt where X was the run number. Thus far in the analysis, the cuts for Run 195 have been used when analyzing other runs. The cuts are listed in Appendix D.

C.3.2 Drift Chamber Coefficients

To determine the coefficients for finding the location of events in the drift chamber, a ROOT macro called WC_coeff.C was written. The macro accepted parameters of run number, drift chamber and plane name, and three initial guesses for the values of the coefficients. The macro used the gMinuit function and a series of releases and holds for the three input parameters to minimize the chi-squared function (Eq. 3.6). The macro returned the best fit values for the coefficients and an uncertainty in each coefficient. The minimized coefficients were saved in /delta00/database with the format of drift chamber and plane name and a file extension .COEFF, as in the example WC1X1POS.COEFF. The output histograms from this macro may be seen in Figure 16.

C.3.3 Determine Drift Distance

The ROOT macro to determine the drift distance for any given drift time was called Integrate.C. It accepted parameters of run number, drift chamber and plane name, and the low and high channel

limits for the integration. The low and high channel limits were determined from histograms of the raw data for the sum of the times from the left and right TFCs. The macro read in the coefficients determined by WC_coeff.C. Integrated was performed by using a loop to sum over the channels from the low channel to the high channel and to save the sum in the drift distance array. This array was saved to /delta00/database in the format of histogram name and a file extension .drift, as in the example WC1X1SUM.drift. Using this look-up table, the drift distance could be determined for any given drift time. A typical plot of the integration may be seen in Figure 17.

C.3.4 Resolution of Left-Right Ambiguity

On which side of the anode wire an event occurred was determined using the ROOT macro OddEven.C. The macro accepted parameters of run number, drift chamber name, and the plane under consideration in each drift chamber (x or y) and read in the coefficients and drift distance tables found with WC_coeff.C and Integrate.C. Histograms of the raw data from the ADC (see Figure 12), as shown in Figure 18, were used to determine the cuts for the center of the valley region. These cuts for each run analyzed were saved in the /delta00/database directory with the format RunX_oddeven.cut where X was the run number. The Run195_oddeven.cut was the default cut file and these cuts may be seen in Appendix D. The macro used these cuts as well as the other data that had been read in to produce plots of the location of events in one plane versus the location of events in that same plane in the drift chamber behind the first. The correct choices for adding and subtracting the drift distance to the anode wire were visually determined, as shown in Figure 20. ROOT macro OddEven_all.C plotted the locations of events for each of the four sets of drift chambers.

C.4 Location of Events with Respect to Beam Line

To determine the location of events with respect to the beam line, plots of x versus y for each drift chamber were made using the ROOT macro called chamber_x_vs_y.C. The macro accepted arguments of run number and drift chamber name and read in the coefficients and drift distance tables found in the two previous macros as well as using the drift distance addition and subtraction configurations just found. The macro used the cuts as well as the other data that had been read in to

produce plots of x versus y for the given drift chamber. Another macro, All_chambers_x_vs_y.C, produced the plots for each of the drift chambers. Plots without the brick were compared to plots with the brick and the anode wires blocked by the bricks were determined. To determine the edge of the location of the brick, a function was written that used three horizontal lines to approximate the edge of the brick in a projection into the x or y plane, as shown in Figure 24. The function, called fitfun.C, was saved in /delta00/macros. Using the same method, the edges of the ΔE scintillator were also fit.

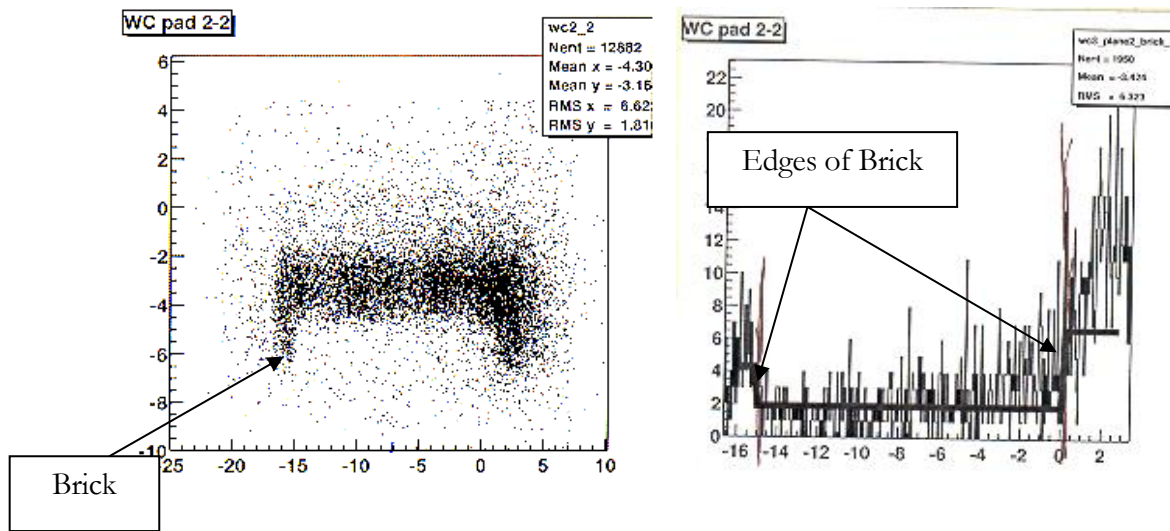


Figure 24. Determining the location of the lead brick in front of the drift chamber. The brick made the sharp cut off in the left plot of the x plane versus the y plane for a front drift chamber. The plot of x versus y is projected onto the x axis in the plot at right and fit with three horizontal lines to determine the location of the brick edge cut-off.

CUTS APPLIED TO DATA

The contents of the default cut files `deltatests_cuts.txt` and `RUN195_oddeven.cut` are included below. Cuts in the `deltatests_cuts.txt` file are the channels bounding the regions of interest in for FERA or CAMAC output. These have been identified by the names given in the Electronics Diagrams in Appendix B. Cuts in the `RUN195_oddeven.cut` file are the center channels of histograms of the output from the ADCs for each drift chamber, such as is given in Figure 18.

`deltatests_cuts.txt`:

Default (Run 195) tests for delta 2000

NTOF1
2000 5000
NTOF2
2000 5000

DE1
-10 10000
DE2
-10 10000

E1
75 1024
E2
75 1024
E3
75 1024
E4
75 1024
E5
75 1024
E6
75 1024
E7
75 1024

E8
75 1024
E9
75 1024
E10
75 1024
E11
75 1024
E12
75 1024

WC1X1L
400 1400
WC1X1R
400 1400
WC1Y1B
300 1300
WC1Y1T
300 1300
WC1X2L
600 1600
WC1X2R
600 1600
WC1Y2B
300 1300
WC1Y2T
300 1300

WC2X1L
200 1800
WC2X1R
200 1800
WC2Y1B
200 1500
WC2Y1T
200 1500
WC2X2L
200 1800
WC2X2R
200 1800
WC2Y2B
200 1500

WC2Y2T
200 1500

WC3X1L
200 1400
WC3X1R
100 1400
WC3Y1B
200 1500
WC3Y1T
100 1500
WC3X2L
100 1400
WC3X2R
150 1500
WC3Y2B
200 1500
WC3Y2T
200 1500

WC4X1L
150 1700
WC4X1R
100 1700
WC4Y1B
400 1800
WC4Y1T
200 1700
WC4X2L
150 1700
WC4X2R
150 1700
WC4Y2B
300 1700
WC4Y2T
300 1600

C1X1OE
200 1800
C1Y1OE
50 900
C1X2OE

100 1800
C1Y2OE
25 600

C2X1OE
200 800
C2Y1OE
200 800
C2X2OE
200 700
C2Y2OE
300 800

C3X1OE
600 1600
C3Y1OE
200 1600
C3X2OE
500 1600
C3Y2OE
400 1200

C4X1OE
400 1050
C4Y1OE
200 1200
C4X2OE
400 1000
C4Y2OE
400 1100

RUN195_oddeven.cut:

These are the odd-even cuts for run 019

WC1X1 1191
WC1X2 745
WC1Y1 319
WC1Y2 220
WC2X1 492
WC2X2 454
WC2Y1 497

WC2Y2 558
WC3X1 1104
WC3X2 1069
WC3Y1 845
WC3Y2 654
WC4X1 742
WC4X2 729
WC4Y1 620
WC4Y2 775

References

-
- [1] The European Physical Journal **C3**, 653 (1998).
 - [2] Ch. Hadjuk *et. al.*, Nucl. Phys. **A405**, 605 (1983).
 - [3] H. Primakoff and S.P. Rosen, Phys. Rev. **184**, 1925 (1969).
 - [4] J.L. Matthews, prepared for the 2nd Workshop on Electronuclear Physics with Internal Targets and the BLAST Detector (1998).
 - [5] C.L Morris *et. al.*, Phys. Lett. **B419**, 25 (1998).
 - [6] A.M. Green, Rep. Prog. Phys **39**, 1109 (1976).
 - [7] E.A. Pasyuk *et. al.*, Los Alamos Neutron Science Center proposal #19981554 (1998).
 - [8] T. Emura *et. al.*, Phys. Lett. **B306**, 6 (1993).
 - [9] H.J. Lipkin and T.-S.H. Lee, Phys. Lett. **B183**, 22 (1987).
 - [10] R.G. Milner and T. W. Donnelly, Phys. Rev. **C37**, 870 (1988).
 - [11] <http://lansce.lanl.gov/facilities/accelerator.htm>.
 - [12] M.S. Livingston and J.P. Blewett, *Particle Accelerators*. New York: McGraw-Hill Book Company, 1962.
 - [13] M.E. Yuly, Ph.D. Thesis, Massachusetts Institute of Technology, 1993.
 - [14] Los Alamos Neutron Science Center Activity Report, 5 (2001).
 - [15] N. Tsoulfanidis, *Measurement and Detection of Radiation*. Washington D.C.: Taylor & Fancis, 1995.
 - [16] C.L. Morris, Nucl. Instr. Meth., **196**, 263 (1982).
 - [17] Indiana University Cyclotron Facility. *XSYS: User Guide to XSYS\IUCF: Introduction, Setup, and Operation*, 1991.
 - [18] Conseil European pour la Recherche Nucleaire. *ROOT: Users' Guide v3.1b*, 2001.